

## Article

# Preparation and Numerical Optimization of TiO<sub>2</sub>:CdS Thin Films in Double Perovskite Solar Cell

Ghazi Aman Nowsherwan<sup>1</sup> , Aurang Zaib<sup>1</sup>, Aqeel Ahmed Shah<sup>2</sup> , Mohsin Khan<sup>1</sup> , Abdul Shakoor<sup>3</sup>, Syed Nizamuddin Shah Bukhari<sup>4</sup>, Muhammad Riaz<sup>1</sup>, Syed Sajjad Hussain<sup>1,\*</sup> , Muhammad Ali Shar<sup>5</sup>  and Abdulaziz Alhazaa<sup>6</sup> 

- <sup>1</sup> Centre of Excellence in Solid State Physics, University of the Punjab, Lahore 54590, Pakistan; ghaziaman.pu@gmail.com (G.A.N.); aurangzaib.cssp@gmail.com (A.Z.); mohsin.cssp@gmail.com (M.K.); mriazkhanbalouch@gmail.com (M.R.)
  - <sup>2</sup> Wet Chemistry Laboratory, Department of Metallurgical Engineering, NED University of Engineering and Technology, Karachi 75720, Pakistan; aqeelshah@cloud.neduet.edu.pk
  - <sup>3</sup> Department of Physics, University of the Punjab, Lahore 54590, Pakistan; abdulphysics2020@gmail.com
  - <sup>4</sup> Department of Basic Science and Humanities, Dawood University of Engineering and Technology, Karachi 74800, Pakistan; nizamuddin@duet.edu.pk
  - <sup>5</sup> Department of Mechanical & Energy Systems Engineering, Faculty of Engineering and Informatics, University of Bradford, Bradford BD7 1DP, UK; m.baloch@bradford.ac.uk
  - <sup>6</sup> Department of Physics and Astronomy, College of Science, King Saud University, Riyadh 11451, Saudi Arabia; aalhazaa@ksu.edu.sa
- \* Correspondence: sajjadh.cssp@pu.edu.pk

**Abstract:** This work focuses on preparing TiO<sub>2</sub>, CdS, and composite TiO<sub>2</sub>:CdS thin films for photovoltaic applications by thermal evaporation. The suggested materials exhibit very good optical and electrical properties and can play a significant role in enhancing the efficiency of the device. Various microscopy and spectroscopy techniques were considered to investigate the optical, morphological, photoluminescence, and electrical properties. FTIR confirms the material identification by displaying some peaks in the fingerprint region. UV Vis spectroscopy yields high transmission (80–90%) and low absorbance (5–10%) within the spectral region from 500 nm to 800 nm for the composite thin films. The optical band gap values for CdS, TiO<sub>2</sub>, and TiO<sub>2</sub>:CdS thin films are 2.42 eV, 3.72 eV, and 3.6 eV. XRD was utilized to analyze the amorphous nature of the thin films, while optical and SEM microscopy were employed to examine the morphological changes caused by the addition of CdS to TiO<sub>2</sub>. The decrease in the bandgap of the composite thin films was determined by the Tauc plot, which is endorsed due to the band tailing effects. Photoluminescence spectroscopy depicts several emission peaks in the visible region when they are excited at different wavelengths, and the electrical measurement enhances the material conductivity. Furthermore, the proposed electron transport materials (TiO<sub>2</sub>, CdS, TiO<sub>2</sub>:CdS) were simulated with different perovskite materials to validate their design by employing the SCAPS-1D program and assess their performance in commercial implementation. The observed results suggest that TiO<sub>2</sub>:CdS is a promising candidate to be used as an ETM in PSC with enhanced productivity.

**Keywords:** thin films perovskite solar cell; electron transport material; titania; cadmium sulphide



**Citation:** Nowsherwan, G.A.; Zaib, A.; Shah, A.A.; Khan, M.; Shakoor, A.; Bukhari, S.N.S.; Riaz, M.; Hussain, S.S.; Shar, M.A.; Alhazaa, A. Preparation and Numerical Optimization of TiO<sub>2</sub>:CdS Thin Films in Double Perovskite Solar Cell. *Energies* **2023**, *16*, 900. <https://doi.org/10.3390/en16020900>

Academic Editor: Long Zhou

Received: 28 November 2022

Revised: 28 December 2022

Accepted: 9 January 2023

Published: 12 January 2023



**Copyright:** © 2023 by the authors. Licensee MDPI, Basel, Switzerland. This article is an open access article distributed under the terms and conditions of the Creative Commons Attribution (CC BY) license (<https://creativecommons.org/licenses/by/4.0/>).

## 1. Introduction

Titanium dioxide (TiO<sub>2</sub>) nanomaterials are renowned for their wide range of applications, such as in the photovoltaic, photocatalytic degradation of pollutants, water purification, solar cell, biosensing, and drug delivery, due to their wide bandgap and good optical and electrical properties [1–6]. Cadmium sulphide (CdS), a semiconductor compound with a direct bandgap of 2.4 eV, has also drawn considerable interest for a variety of applications, including in photovoltaic devices, photodetectors, light emitting diodes (LEDs), optical filters, and transistors [7,8]. TiO<sub>2</sub>:CdS thin films may be produced

using various techniques, including the sol-gel method, chemical vapor deposition (CVD), and physical vapor deposition (PVD). However, due to them being simple and affordable, thermal evaporation was chosen by the researchers, and it has received a lot of attention due to its capability as an electrode, electron transport material (ETM), and transparent conducting oxide film (TCO) in solar cells [9–12].

Photovoltaic (PV) development has been exponentially accelerated by the global, escalating energy demand. PSCs have emerged as a promising PV technology due to their excellent optical and electronic properties. Materials that are made of perovskite have been well understood for a long time. Kojima et al. from the Tokyo-based collaboration of Tsutomu Miyasaka created the first perovskite solar cell in 2006 with a PCE of 2.2% [13]. After a few years, they enhanced it to 3.8% [14]. In 2011, a perovskite cell with a nanocrystal size of 2–3 nm attained an efficiency (PCE) of 6.54% within two years [15]. Although there has been a tremendous increase in PSC efficiency and productivity over the previous decade, the current PSC efficiencies have not yet exceeded the maximum theoretical limit [16,17]. One-dimensional (or 1D) nanostructured oxides, such as rutile TiO<sub>2</sub>, ZnO, and SnO<sub>2</sub> nanorods, have been suggested to be potentially better ETMs for highly efficient perovskite devices since the 1D structure theoretically benefits both charge transport and light transmission [18]. In photovoltaic (PV) applications, anatase TiO<sub>2</sub> performs better than rutile TiO<sub>2</sub> does [19] due to its increased capacity to transport electrons and more acceptable energy levels. However, because of their simplicity in their synthesis, 1D rutile TiO<sub>2</sub> nanostructures have been widely employed as ETMs in PSCs. The efficiency of the PSC device is also significantly impacted by the ETM's design and fabrication [20].

In PSCs, TiO<sub>2</sub> is the most widely used ETM, [21,22] although the use of other oxide materials, such as SnO<sub>2</sub> [23], ZnO [24,25], Zn<sub>2</sub>SnO<sub>4</sub> [26], and BaSnO<sub>3</sub>, [27,28], TiO<sub>2</sub>/SnO<sub>2</sub> [29], TiO<sub>2</sub>/ZnO [30], and NiO/TiO<sub>2</sub> [31], has also been reported in the literature. Several reports also detail the use of CdS as an ETM in perovskite solar cells and as a buffer layer in CIGS- and CdTe-based solar cells [32–35]. Numerous TiO<sub>2</sub> nanostructures are superior perovskite scaffolds. The extraction of photoinduced electrons from perovskite and subsequent transport of those electrons to an electrode are crucial functions of these TiO<sub>2</sub> nanostructures. It was discovered that the TiO<sub>2</sub> nanostructure's crystal phase, morphologies, wettability, and surface states significantly impact the photovoltaic performance of PSCs.

SCAPS-1D has been extensively utilized to examine thin film and planar solar cells to discover how the cell architecture and material properties impact the cells' performance. Lin et al. designed the PSC structure without the hole transport layer by utilizing the SCAPS simulator and achieved more than 15% efficiency under optimized conditions [36]. S. Chakraborty et al. evaluated the impact of temperature and thickness variations on the performance of a Cs<sub>2</sub>TiX<sub>6</sub>-based PSC. They found that the active layer thickness and temperature significantly impacted the efficiency of perovskite solar cells [37]. Karthick et al. fabricated formamidinium-based perovskite cells and studied the effect of series and shunt resistance on the performance of PSC. They obtained a maximum PCE of 21.4%, theoretically, and 15.1%, practically [38]. Nowsherwan et al. made a double perovskite solar cell that did not use a lead component. They studied the effects of different HTMs under the best conditions and obtained an efficiency of more than 24% [39]. Abdel Aziz et al. evaluated and modeled tin-based PSC and obtained a PCE of 14.03% under optimized parameters [40]. Sajjad Hussain et al. designed a lead-free double PSC that yielded a productivity of 24.98% at a photoactive layer thickness of 300 nm [41]. Kumar et al. structured tin-based lead-free PSC and obtained an enhanced output parameters short-circuit current density ( $J_{sc}$ ) of 31.20 mA/cm<sup>2</sup>, an open-circuit voltage ( $V_{oc}$ ) of 1.81 V, a fill factor (%FF) of 33.72%, and a power conversion efficiency (PCE) of 19.08% after evaluating the best possible parameters [42]. K. Sobayel et al. studied the defects in a tin-based PSC constructed using the SCAPS program and achieved a PCE value of more than 20% under optimum conditions [43]. With the aid of SCAPS, S.Z. Haider and colleagues constructed perovskite solar using CuI as a hole-extracting material that gives a PCE of 21.32% and an FF of 84.53% under optimum conditions [44].

The primary goal of this research was to investigate the optical and electrical properties of  $\text{TiO}_2$  and  $\text{TiO}_2\text{:CdS}$  thin films produced by thermal evaporation to evaluate their efficacy as a viable electron transport medium. The purpose of incorporating CdS into  $\text{TiO}_2$  was to enhance the transmission, photoconductivity, and optical bandgap to generate a more efficient electron transport layer for the PSC. Moreover, we modelled the suggested electron transport materials ( $\text{TiO}_2$ , CdS,  $\text{TiO}_2\text{:CdS}$ ) with several perovskite materials using the SCAPS-1D program to confirm their design and assess their performance in a practical application.

## 2. Experimental

### 2.1. Sample Preparation

Thermal evaporation is carried out using Edward Coater 306 to fabricate the required thin films. It is a type of physical vapor deposition technique that passes an electric current through a source at low pressure. The schematic representation of thermal evaporation is represented in Figure 1. Evaporation is achievable by producing contact between the source material concerning a surface that is resistively heated through the passage of current [45]. The cleaning of the glass substrates was performed in different steps. Firstly, the glass substrates were cleaned with acetone in an ultrasonic bath for 15 min. Next, these substrates were placed in the beaker containing IPA and kept in the ultrasonic bath for 15 min [46]. The substrates were dried using a nitrogen gun to avoid contamination and eliminate the IPA (Iso Propyl Alcohol) on the substrates, and then, they were placed on a substrate holder.  $\text{TiO}_2$  and  $(\text{TiO}_2)_{0.7}\text{:CdS}_{0.3}$  (0.25 g) was put in a tungsten boat, and then deposited using the thermal evaporation process by applying an electric current of 50A through a filament at a pressure of about  $2 \times 10^{-5}$  Torr. The substrate was placed directly above the source at a distance of about 22 cm. The deposition time for all of the samples was maintained at 5 min. The main steps involved in the fabrication of thin films are illustrated in Figure 2.

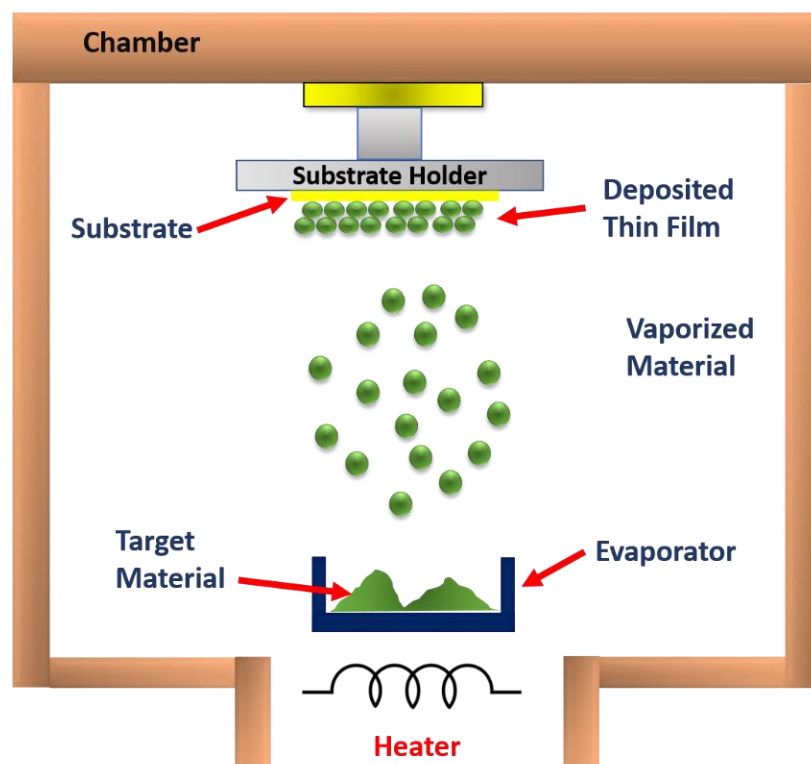
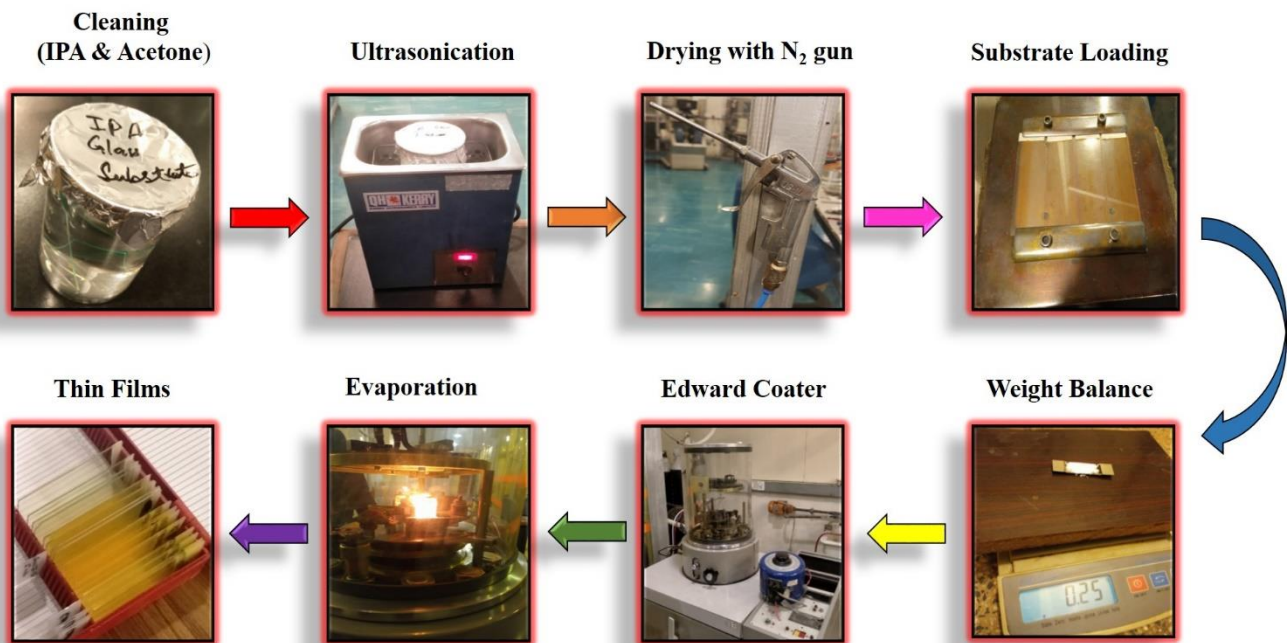


Figure 1. Schematic diagram of thermal evaporation.



**Figure 2.** Thin film preparation steps.

## 2.2. Characterization

UV-Vis Shimadzu 1800 was utilized to determine the optical properties of the deposited thin films. This technique measures a sample's absorbance and scattering of light [47,48]. The resulting spectrum has a 200–1200 nm wavelength range. It provides data on bandgap, absorption, and transmission. The X-ray diffraction technique examines the crystal structure of the deposited thin films. The Cu K $\alpha$  radiation at the 1.5406 Å wavelength was used to evaluate X-ray diffraction data recorded using the Bruker D8 Advance [49]. The Xpert high score program was used to evaluate the crystal structure of the deposited thin films. The Agilent Carry 630 FTIR spectrometer was used to perform the FTIR. It is a quick and non-destructive method for identifying the presence of chemical bonding in a substance [50,51]. This method typically captures the spectra between 400 and 4000 cm<sup>-1</sup>. The detector's output signal acts as the specimen fingerprint and aids in identifying the substance.

The FS5 spectrofluorometer was used to study the deposited thin film's photoluminescence characteristics [51,52]. It uses fluorescence spectra to provide information regarding the bandgap, chromaticity, and excitation and emission spectra for the substances with a certain composition. The output is calculated by graphing the photon count against the emission wavelength. It encompassed the 200–1000 nm spectral range. Every aspect of the FS5 is fully computer controlled, including the excitation and emission monochromators, bandwidth, and xenon arc lamp. An optical microscope (NOVEX HOLLAND) associated with an integrated CCD camera was used to investigate the micro-topography of the deposited thin films at a magnification of 1000 $\times$ . The magnification of tiny samples is often accomplished using a lens system and visible light. Additionally, standard light-sensitive cameras can be used to capture micrographs using an optical microscope [53,54]. The SEM analysis was performed using the ZEISS instrument and TESCAN Mira 3 field emission microscope. It is the most often used surface analysis approach for generating high-resolution surface texture and roughness images. The Van der Pauw (VDP) measures the electrical parameters (i.e., average resistivity, mobility, and Hall coefficient) by applying current and monitors voltage along the sample's perimeter. It enables the evaluation of irregular forms and more typical structures [55].

### 3. Numerical Modeling of Double Perovskite Solar Cell

Herein, SCAPS (version 3.3.07) was used to design and analyze the simulated photovoltaic cell in various segments [38]. The user is given access to several panels inside the application, enabling them to adjust the settings and form opinions on the outcome. Specifically, Poisson's and Continuity differential equations serve as the foundation for this software application. These can be mathematically written as:

$$\frac{d}{dx} \left( \epsilon(x) \frac{d\varphi}{dx} \right) = q [p(x) - n(x) + N_{d+}(x) - N_{a-}(x) + p_t(x) - n_t(x)] \quad (1)$$

$$\frac{dp_p}{dt} = G_p - \frac{p_p - p_{p0}}{\tau_p} - p_p \mu_p \frac{dE}{dx} - \mu_p E \frac{dp_p}{dx} + D_p \frac{d^2 p_p}{dx^2} \quad (2)$$

$$\frac{dn_p}{dt} = G_n - \frac{n_p - n_{p0}}{\tau_n} + n_p \mu_n \frac{dE}{dx} + \mu_n E \frac{dn_p}{dx} + D_n \frac{d^2 n_p}{dx^2} \quad (3)$$

where:

- $\epsilon$  = dielectric constant;
- $q$  = electron charge;
- $G$  = Rate of generation;
- $D$  = Coefficient of diffusion;
- $\varphi$  = Electrostatic potential;
- $E$  = Electric field;
- $\mu_n$  = Electron mobility;
- $\mu_p$  = Hole mobility;
- $x$  = thickness;
- $p(x)$  = allowed concentration of the holes;
- $n(x)$  = allowed concentration of the electrons;
- $p_t(x)$  = captured holes;
- $n_t(x)$  = captured electrons;
- $N_{d+}$  = Ionized doping concentration of the donor;
- $N_{a-}$  = Ionized doping concentration of the acceptor;
- $\tau_p$  = lifetime of the hole;
- $\tau_n$  = lifetime of the electron.

Together with the necessary boundary conditions at the interfaces and contacts, these equations produce a system of linked differential equations in the bulk of the layers. This system's steady state and small signal solutions are computed numerically using SCAPS.

The solution of these differential equations is accomplished by using Gummel-type iteration and numerical differentiation methods, which is the basic concept of this application [56,57]. The numerical panel's convergence settings include the parameters of this technique. At the start point, each computation begins, given that there is no potential drop over the structure and that the quasi-Fermi levels are all at 0. It is employed as a first estimation, with no illumination and voltage to being used obtain to the equilibrium condition. Under the working point conditions, this equilibrium condition is utilized as an initial approximation to compute the solution. However, the short circuit condition is estimated in a preliminary stage to act as the next initial assumption when the lighting is turned on.

The heterojunction structure that has been carried out in this study is a double perovskite solar cell (d-PSC) cell structure that includes the perovskite material as a photo-harvesting layer. The device contains an absorber layer, HTL (Spiro-MeOTAD), an ETL (TiO<sub>2</sub>, CdS, TiO<sub>2</sub>:CdS), transparent conducting oxide (FTO), and a metal contact (Au), as illustrated in Figure 3.

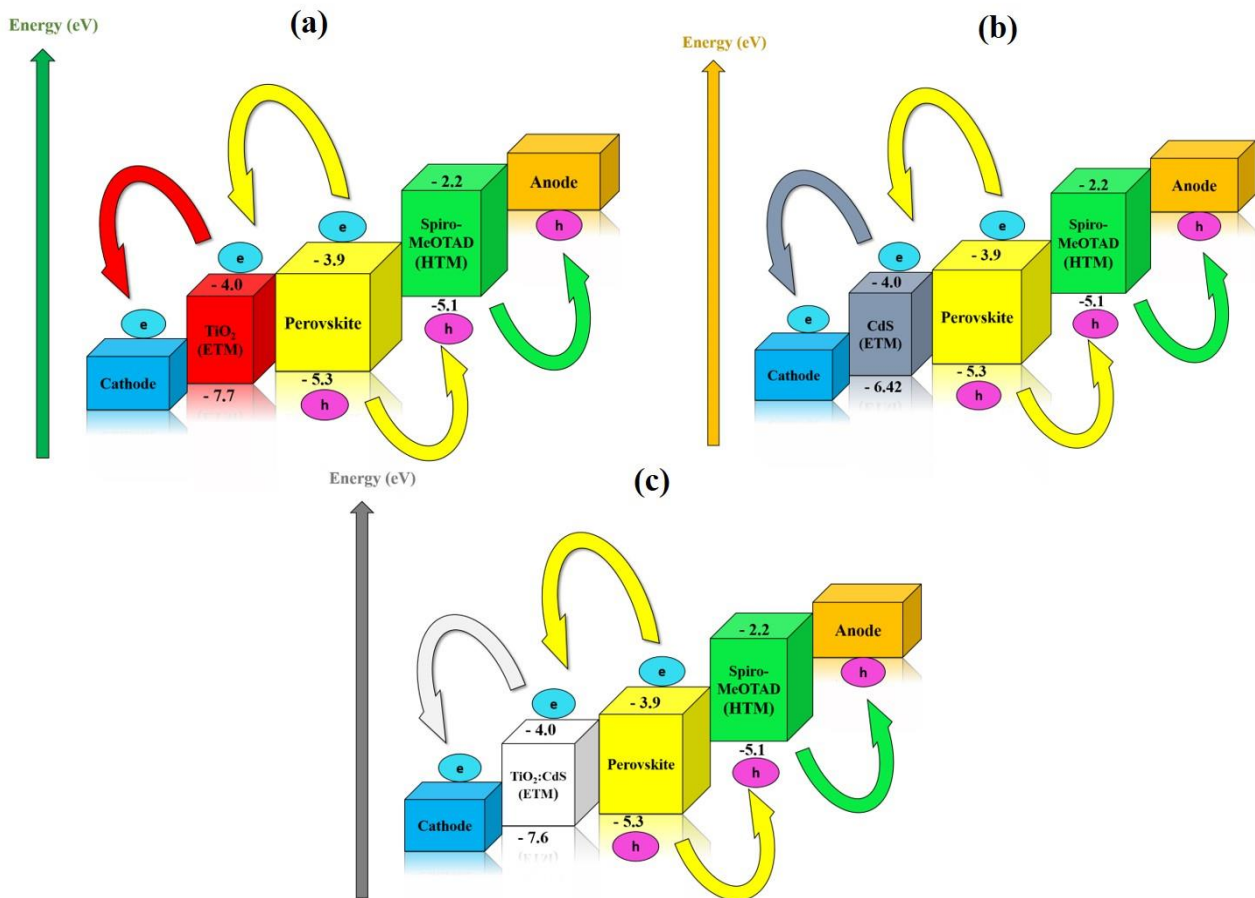


Figure 3. Energy band diagram of PSC with ETM (a)  $\text{TiO}_2$ , (b)  $\text{CdS}$ , and (c)  $\text{TiO}_2:\text{CdS}$ .

## 4. Results and Discussion

### 4.1. UV-Vis Results

The transmission and absorption spectra acquired in the 200–1200 nm wavelength range were used to evaluate the optical characteristics of the films placed on the glass substrate. Figure 4a–c displays the combined transmission and absorption spectra of  $\text{TiO}_2$ ,  $\text{CdS}$ , and  $\text{TiO}_2:\text{CdS}$  thin film. It was observed that with the increase in the wavelength, the transmission increases and the absorption decreases for all of the samples due to a decrease in the incident energy which no longer satisfies the absorption condition. The maximum transmission values observed in the case of  $\text{CdS}$  and  $\text{TiO}_2$  were 86% and 70%, respectively, while transmission in the visible area increased substantially to 89% in the case of  $\text{TiO}_2:\text{CdS}$  due to structural and morphological changes after  $\text{CdS}$  inclusion in  $\text{TiO}_2$ . It was also observed that the fundamental absorption edge of  $\text{TiO}_2:\text{CdS}$  was shifted towards the high wavelength after incorporating  $\text{CdS}$  into  $\text{TiO}_2$ . The pure  $\text{TiO}_2$  film exhibited high absorption in the UV range, and it did not significantly absorb the visible light [58].

However, the  $\text{TiO}_2:\text{CdS}$  thin films exhibited the highest transparency in the visible region, which is ascribed to the addition of  $\text{CdS}$  and agrees with other earlier results [59], making them suitable for use as an ETM in solar cells. In contrast,  $\text{CdS}$  has a high absorbance in the ultraviolet region, but it has a low absorption in the visible region. It also has high transmittance in the visible range. We normally want a material with an excellent transparency and bandgap for photovoltaic applications. Therefore,  $\text{TiO}_2:\text{CdS}$  thin films can be employed as a potential alternatives to other ETMs with enhanced productivity. These results are essential for optoelectronics applications, especially solar cells.

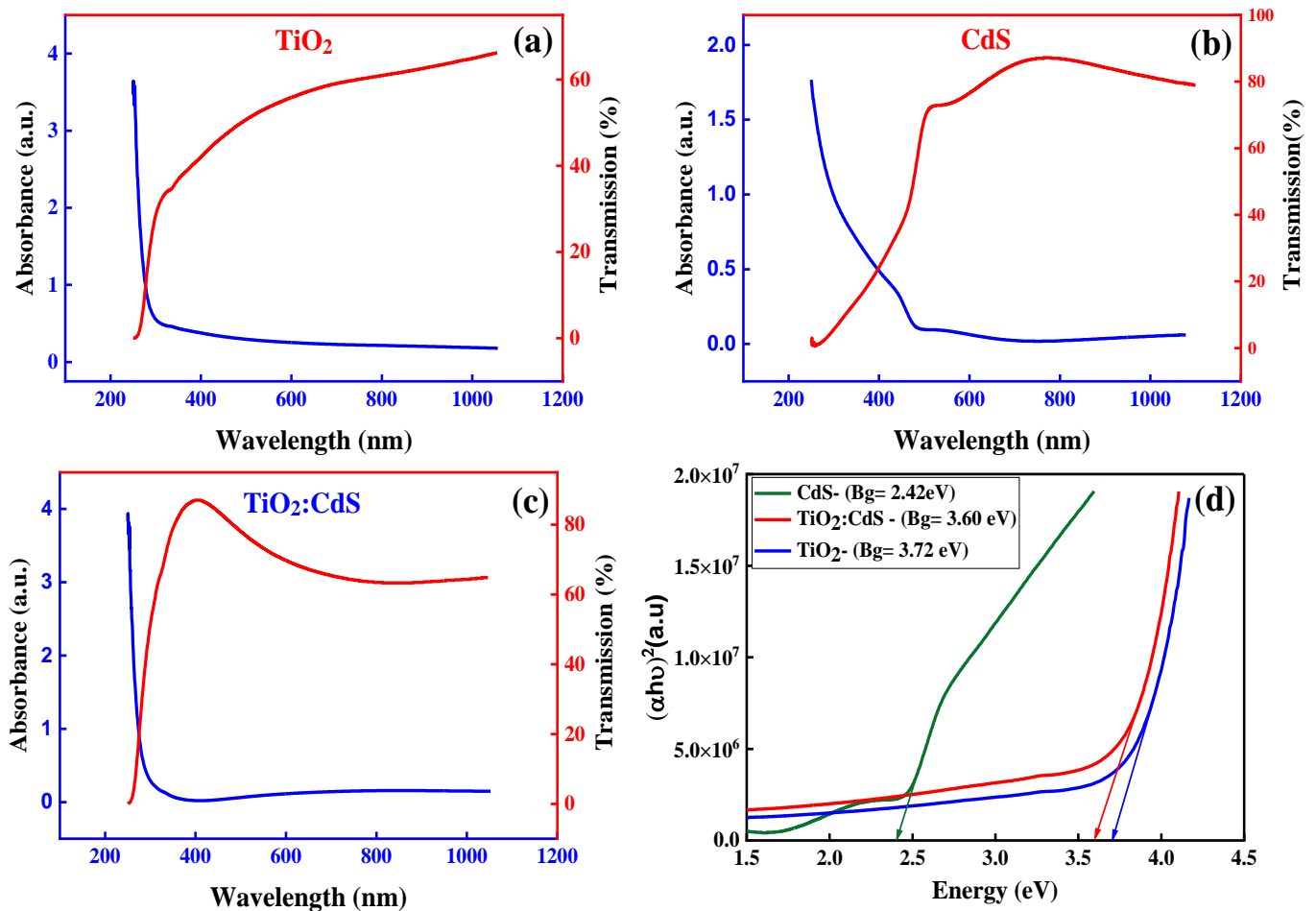


**Figure 4.** (a) Absorbance and transmission spectra of TiO<sub>2</sub>, (b) absorbance and transmission spectra of CdS, (c) absorbance and transmission spectra of TiO<sub>2</sub>:CdS, and (d) Tauc plot (band gap) of prepared samples.

#### Tauc Plot

The Tauc plot is a method used to estimate the band gap of deposited thin films by following the relation [60]:

$$\alpha h\nu = A(h\nu - E_g)^n \quad (4)$$

where  $\alpha$  is the absorption coefficient;  $h\nu$  is incident energy;  $A$  is material constant;  $n$  corresponds to the transition ( $n = 0.5$  for direct allowed transition,  $1.5$  for direct forbidden transition,  $2$  for indirect allowed transition, and  $3$  for indirect forbidden transition). Herein,  $n$  is assumed as  $0.5$  for determining the band gap of deposited thin film.

The Tauc plot (Figure 4d) displays the plot between the  $(\alpha h\nu)^2$  and the energy, which is an efficient approach for determining the optical band gap by conducting extra linear plotting. The band gap values for CdS and TiO<sub>2</sub> were  $2.42$  and  $3.72$  eV, respectively. The band gap values observed for TiO<sub>2</sub> and CdS are consistent with those of previous studies [61–63]. The band gap value slightly decreased from  $3.72$  eV to  $3.60$  eV after adding CdS into TiO<sub>2</sub>. This might be due to the localization of the energy levels and the band tailing effects caused by overlapping the wave function of the impurity atoms with the wave function of the host material's atoms.

#### 4.2. XRD Analysis

The Bruker D8 discover diffractometer equipment with Cu K $\alpha$  X-rays with a wavelength of  $1.5406$  Å was utilized to conduct the structural analysis of the nano-powder and thin films of TiO<sub>2</sub> and CdS. The data were collected with a collection step size and time

of 0.02 degrees and one second, respectively. The data were indexed with the help of an analytical procedure, which involved comparing them to a standard reference pattern contained within the Xpert high score library.

Figure 5a depicts the XRD pattern of TiO<sub>2</sub> nano-powders and thin films produced on a glass substrate. It was discovered that the XRD pattern of the nano-powders of TiO<sub>2</sub> contains anatase and rutile phases, which were used in the deposition of the thin films. The XRD patterns revealed that TiO<sub>2</sub> in the anatase phase exhibits significant diffraction peaks at 25°, 48°, and 75° and weak peaks at 38° and 62.6°, while the rutile phase of TiO<sub>2</sub> was validated with strong diffraction peaks at 27.44° and 54.4° and weak peaks at 36°, 41.32°, and 68.56° [64], which is in accordance with JCPDS card nos. 01-071-1167 and 01-076-0649, respectively. The deposited thin films of TiO<sub>2</sub> showed no peaks, and instead, we recorded diffused XRD profiles because of the amorphous nature of the glass. It could be due to a lattice mismatch between the substrate and the deposited thin films. The XRD pattern of the CdS nano-powders and thin films formed on a glass substrate is depicted in Figure 5b. The results show that the films deposited on glass are amorphous due to the lattice's disorientation and the glass's amorphous nature [65]. In contrast, the nano-powder of CdS exhibits a hexagonal wurtzite structure due to the presence of the peaks corresponding to the planes at the (111), (220), (300), and (311) orientations. Which is consistent with JCPDS card no. 01-080-0006 [66].

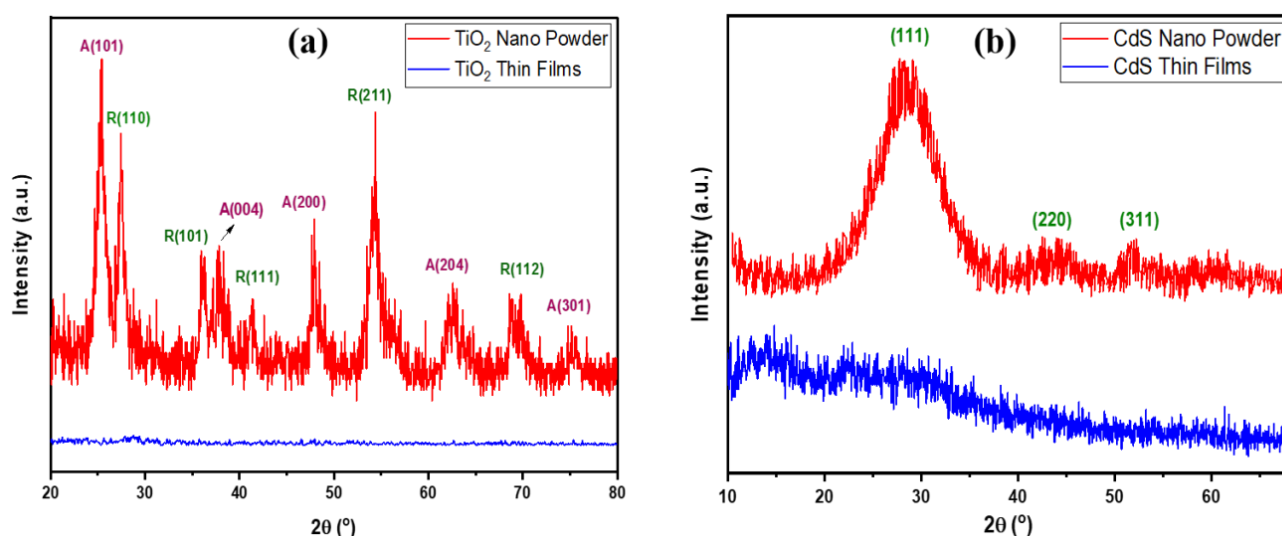


**Figure 5.** (a) XRD pattern of TiO<sub>2</sub> nanopowder and thin film; (b) XRD pattern of CdS nanopowder and thin film.

#### 4.3. FTIR Results

The characteristic peaks of the FTIR spectra along the vibrational mode of TiO<sub>2</sub>, CdS, and TiO<sub>2</sub>:CdS are illustrated in Figure 6. An FTIR spectrometer was used to analyze the interaction of the bonds in the deposited thin films of the TiO<sub>2</sub> and CdS composite. The range of the instrument was from 400 cm<sup>-1</sup> to 4000 cm<sup>-1</sup>. Figure 6 depicts the typical peaks of the FTIR spectra along the vibrational mode of TiO<sub>2</sub>, CdS, and TiO<sub>2</sub>:CdS. The faint absorption band at about 3700 cm<sup>-1</sup> is attributed to the OH stretching vibration of water molecules and the moisture in the processed samples. The modest and faint peak at about 1400 cm<sup>-1</sup> is due to the existence of water molecules with H-O-H bending vibrations. Since sulfur is considered to be a possible H-bond acceptor, the signal at 1646 cm<sup>-1</sup> may have resulted from the -OH bond bending vibrations. A broad peak shows the significant interaction of CdS with the water molecules at 2135 cm<sup>-1</sup>, which reflects the stretching vibration of the -OH bond. The band at 1361 cm<sup>-1</sup> was identified as a typical vibration band of CO ions. Strong band positions in the region of 900–1100 cm<sup>-1</sup> may result from the sulphate group's stretching vibrations. The material peak detected at 748 cm<sup>-1</sup> corresponds

to the stretching mode of the Cd-S bond [67,68]. The broad band at below  $1000\text{ cm}^{-1}$ , with minimum values of  $670\text{ cm}^{-1}$  and  $522\text{ cm}^{-1}$ , can be attributed to the typical Ti–O and Ti–O–Ti stretching and bending vibrational modes of  $\text{TiO}_2$ , respectively, as determined by prior published research [69,70]. In contrast, the peaks at  $1976$  and  $1964\text{ cm}^{-1}$  are attributable to O–H stretching vibrations.

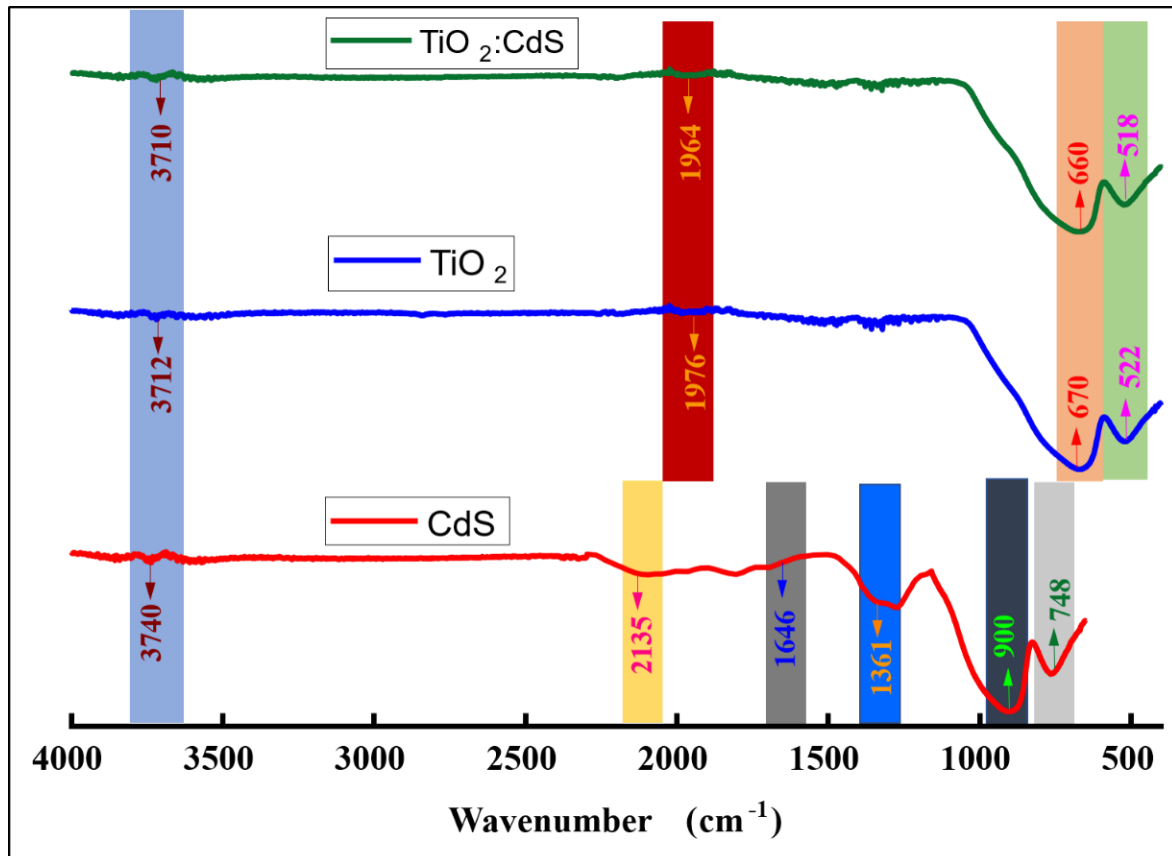


**Figure 6.** FTIR spectra for deposited thin films.

In addition, it is very discernible from the figure that with the addition of CdS, variations in the peak intensity, peak broadness, and peak location occurred. These might be attributed to the interaction of CdS in the  $\text{TiO}_2$  lattice. The figure also demonstrates that the interaction of CdS with  $\text{TiO}_2$  resulted in a change in the bond length and the mass of the molecule, which caused the related peaks to move towards lower wavenumbers.

#### 4.4. Optical Microscopy

An optical microscope was used to conduct a morphological analysis of the  $\text{TiO}_2$ , CdS, and composite  $\text{TiO}_2$ :CdS thin films, which is recorded in microns. Figure 7a exhibits the granular-like morphology of the CdS thin films. In contrast, Figure 7b depicts a homogenous  $\text{TiO}_2$  coating that was applied to the glass substrate, with particles scattered equally throughout the whole surface. The surface morphology of the composite thin films changed as the CdS content increased, as seen by the dark patches in Figure 7c, whereas the pure  $\text{TiO}_2$  films had a bright yellow appearance. The dark spots in the micrographs caused by the increased CdS concentration and grain size are supported by particle accumulation.

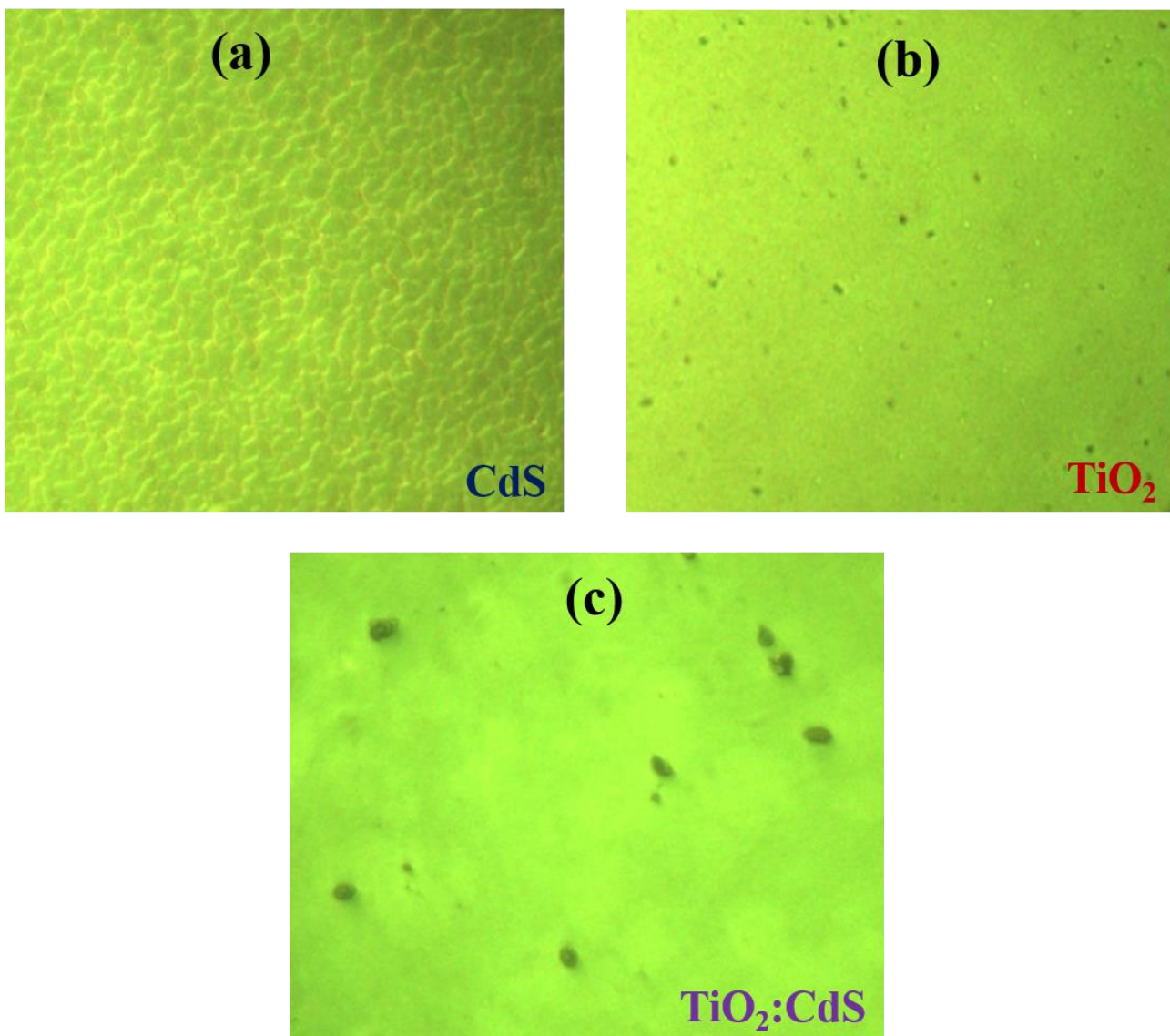


**Figure 7.** Optical microscopy of (a) CdS, (b) TiO<sub>2</sub>, and (c) TiO<sub>2</sub>:CdS thin films at 1000 $\times$ .

#### 4.5. SEM Analysis

The SEM analysis was carried out at different magnifications with accelerating voltages of 20 KV for CdS and 10 KV for the TiO<sub>2</sub> and TiO<sub>2</sub>:CdS thin films. Figure 8a–f shows an SEM image of the CdS, TiO<sub>2</sub> and TiO<sub>2</sub>:CdS thin films prepared by thermal evaporation. It is illustrated that the CdS thin films comprise homogenous spherical shapes that are similar to grains and have a dense morphology that covers the entire glass substrate, while the TiO<sub>2</sub> thin films have a surface that is composed of non-porous, non-uniform spherical grains and a structure that varies in size. The size of the particles was estimated using Image J software: it was observed that the surface is composed of regular-sized agglomerated particles of ~100–150 nm. On the other hand, the TiO<sub>2</sub>:CdS thin films show a coarser surface, with clusters and agglomerations of grains.

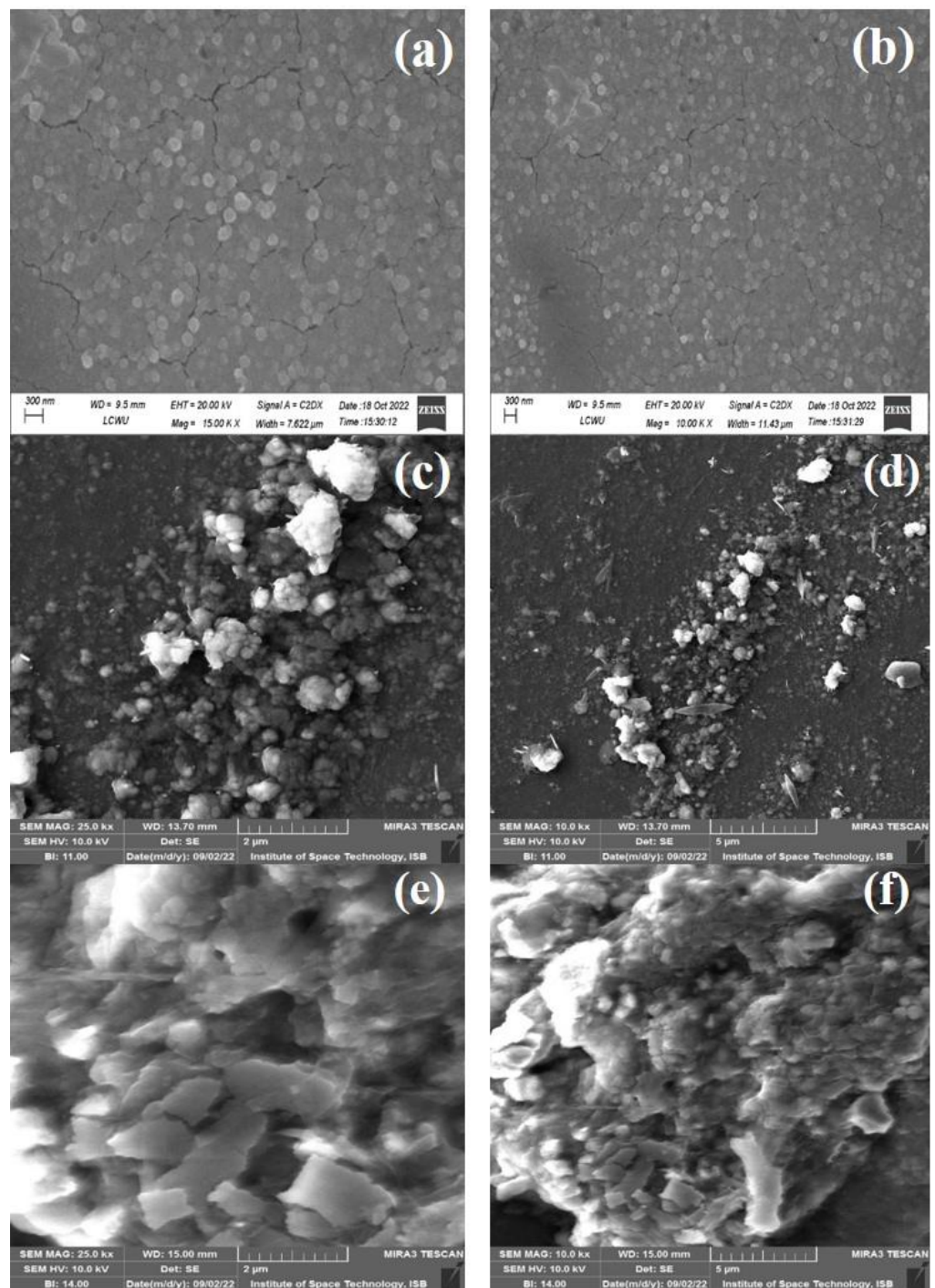


**Figure 8.** SEM microscopy of (a,b) CdS, (c,d) TiO<sub>2</sub>, and (e,f) TiO<sub>2</sub>:CdS thin films.

#### 4.6. Photoluminescence (PL) Analysis

To examine the sample's photoluminescence (PL) properties, the Spectrofluorometer FS5 was used, with a xenon arc lamp acting as an excitatory source. Different emission spectra were obtained using different excitation wavelengths, as shown in Figures 9 and 10. It can be visualized from the PL spectra (Figure 9) that most of the emission peaks were observed in the visible region. The emission peak at 366 nm was due to the recombination of free excitons, and it was in the ultraviolet region. The high intensity of emission peaks observed at 401 nm is due to the radiative recombination of self-trapped exciton

(STE) [71,72]. It is a condition where the electron-hole pair loses the ability to move across the crystal lattice.

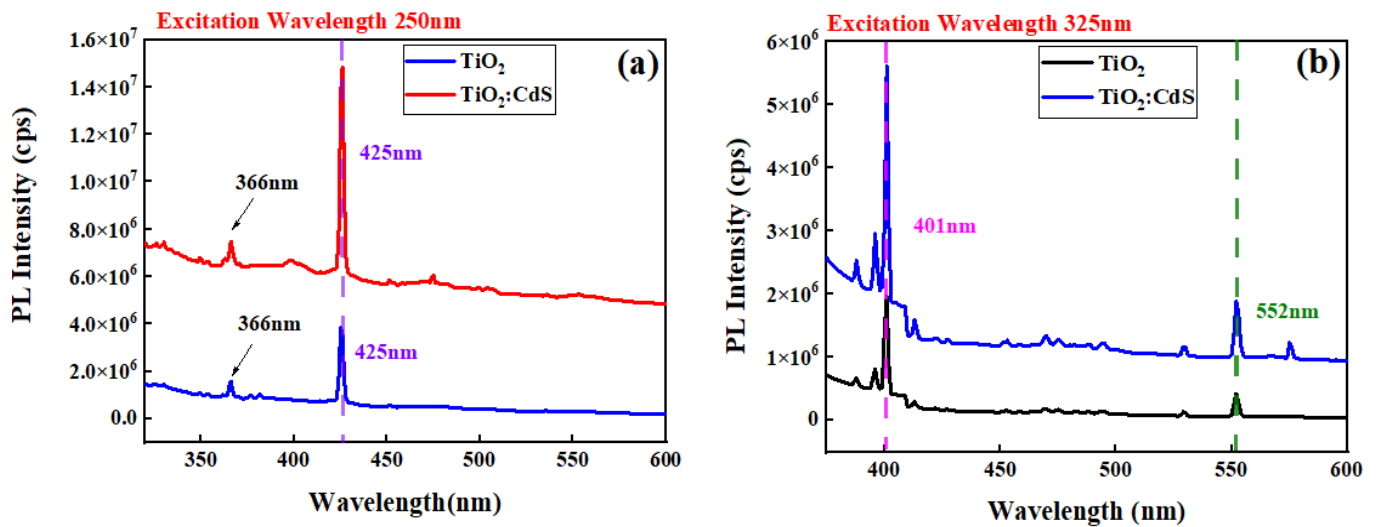


Figure 9. (a) PL spectra of  $\text{TiO}_2$  and  $\text{TiO}_2:\text{CdS}$  at 250 nm excitation wavelength; (b) PL spectra of  $\text{TiO}_2$  and  $\text{TiO}_2:\text{CdS}$  at 325 nm excitation wavelength.

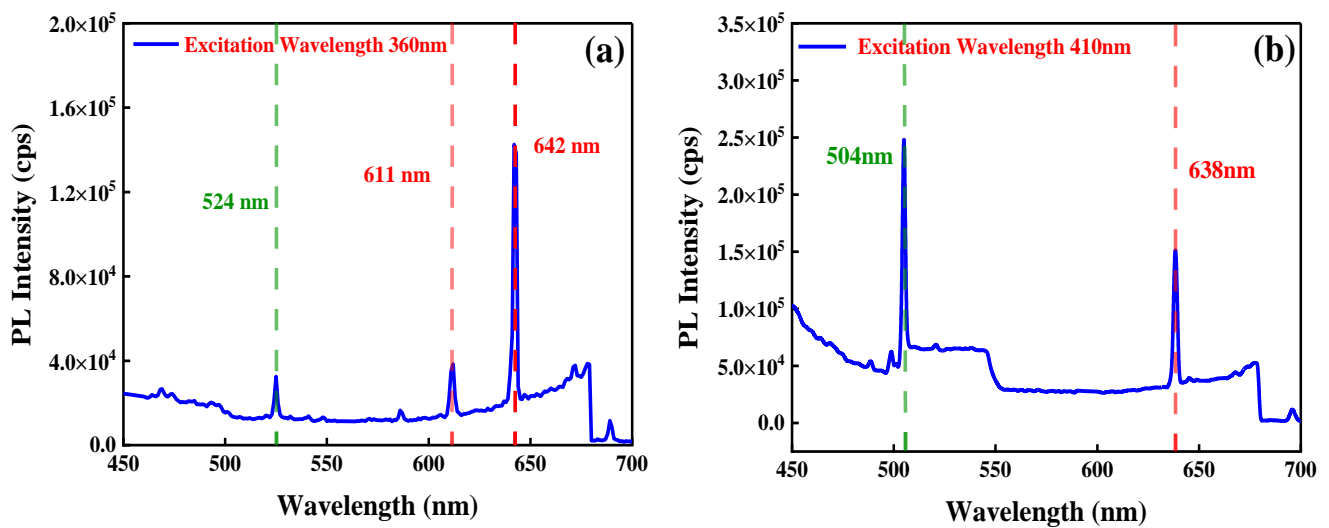


Figure 10. (a) PL spectra of CdS at 360 nm excitation wavelength; (b) PL spectra of CdS at 410 nm excitation wavelength.

In contrast, a well-defined emission occurs at 425 nm due to the low indirect transition or presence of shallow transitions trapped near the band edge [73,74]. Both of the samples exhibit a green luminescence spectrum at 552 nm, which is consistent with the luminescence spectra of single and polycrystalline  $\text{TiO}_2$  that has been published in the literature [75,76]. The peak intensity is also seen to rise following the addition of CdS into the  $\text{TiO}_2$  thin films due to a reduction of the band gap. The increase in the peak intensity is endorsed due to the band-tailing effects, which enhance the band-to-band recombination of the excited electrons. There are several other reports related to oxygen vacancy defects at the shallow levels [77,78].

Figure 10a depicts the CdS film emission spectra at an excitation wavelength of 360 nm. Emission peaks were observed at 524 nm, 610 nm, and 642 nm. The shift from the donor levels to the valence band is considered to be represented by the peak at 524 nm. The traps and/or surface states are responsible for the peak at 610 nm. A transition in the conduction

band between the interstitial Cd donor and acceptor atoms could have caused this emission. The peak at 642 nm in the PL spectra is attributable to the transition caused by CdS, and it is associated with sulfur vacancies [79,80].

Figure 10b depicts the PL spectra of the CdS thin films that were excited at the wavelength at 410 nm. Several emission peaks were observed at different wavelengths. The inter-band transitions are responsible for the 504 nm emission. In general, S-vacancy donors transitioning to the valence band and donor-acceptor pairing recombinations caused the peak. The red emission band at 638 nm in the PL spectra corresponds to a vacancy defect in CdS [79,81].

#### 4.7. Resistivity Measurement

The Van der Pauw technique tests the resistivity of CdS, TiO<sub>2</sub>, and their composite TiO<sub>2</sub>:CdS thin films. The voltage changes are monitored at various points by supplying a 1 mA current at multiple points with a magnetic field of 0.2 T. The average resistivity is calculated using the values of  $2.7 \times 10^4$  ohm-cm,  $2.4 \times 10^{-2}$  ohm-cm, and  $1.2 \times 10^{-2}$  ohm-cm for CdS, TiO<sub>2</sub>, and TiO<sub>2</sub>:CdS, respectively. Pure TiO<sub>2</sub> has been shown to have higher resistivity than TiO<sub>2</sub>:CdS thin films do, which is supported by incorporating CdS into TiO<sub>2</sub>. As the resistance decreases, the conductivity increases, thereby improving the electron transportation at the interfaces. This could be due to the decrease in the band gap. This indicates it is a prospective candidate that can be used as an ETM in photovoltaic devices, notably PSC.

#### 4.8. J–V Comparison between Different ETMs and Perovskite Materials

In this research study, we used different perovskite materials (CH<sub>3</sub>NH<sub>3</sub>PbI<sub>3</sub>, Cs<sub>2</sub>BiCuI<sub>6</sub>, (FA)<sub>2</sub>BiCuI<sub>6</sub>, and (MA)<sub>2</sub>BiCuI<sub>6</sub>) as an absorber material for PSC. These materials exhibited fine optoelectronic properties such as a high absorbance, low bandgap, high charge transfer, and higher optical conductivity. Herein, we have observed the effect on the performance of PSC by incorporating different electron transport materials (ETM) that we have proposed in this study. According to our findings, double perovskite without lead can be a workable replacement for PSC, and it could even be used in creating PSCs for future generations, even though the lead-based perovskite material has substantially better efficiency rates. However, we normally do not use lead-based material due to toxicity and stability considerations. On the other hand, there are no such issues with double lead-free perovskite. As a result, it can be employed as a photo-harvesting material in future generations of PSCs.

Experimentally, the efficiency of a perovskite solar cell without lead has not surpassed 10%. On the other hand, it has been theorized that certain lead-free double perovskite materials have PCE levels that are greater than 20%. These materials have not yet been subjected experimentally, but their optical, electrical, structural, and other properties are being investigated through density functional theory (DFT). Herein, we modelled a handful of these materials and analyzed their performance characteristics, which were similar to those of typical perovskite-based materials. These materials exhibit unique optoelectronic properties, and they may potentially replace conventional lead-based perovskite materials in future solar cells. This study's major objective was to analyze the productivity of d-PSC with various ETMs and find out which perovskite and ETM generates the maximum productivity.

All of the simulation settings for the structure's layers were taken from the research presented in [36,39,41,43,82–85]. Tables 1 and 2 provide a comprehensive summary of each of the essential simulation constraints employed in this simulation.

To simplify the device modelling, absorption profiles for all of the layers were added to a simulation that was taken from several works of literature [86–89] to expedite the process. This device model features two interface defect layers, which are indicated by the letters IL1 (ETM/Photoactive Layer) and IL2 (Photoactive Layer/HTM), to produce a more realistic depiction of the device. The AM1.5G spectrum was employed in this device modelling; its effective temperature was adjusted at 300 K. Additionally, all of the operating

point settings and numerical factors were maintained at their actual value. The range of scanning voltage was set to a range of from zero to one volt. The above parameters were utilized throughout this program to run all of the simulations.

**Table 1.** Material parameters set in simulation.

Parameters	FTO [36,41,43,82]	TiO <sub>2</sub> , CdS, TiO <sub>2</sub> :CdS [41,43,82,85]	Perovskite [26,39,41,43,82,87]	Spiro-MeOTAD [36,39,41,43]
Thickness (nm)	200	50, 50, 50	200	150
Acceptor Density (cm <sup>-3</sup> )	0	0, 0, 0	0	10 <sup>18</sup>
Donor Density (cm <sup>-3</sup> )	10 <sup>19</sup>	10 <sup>17</sup> , 10 <sup>17</sup> , 10 <sup>18</sup>	10 <sup>17</sup>	0
Bandgap (eV)	3.5	3.72, 2.42, 3.6	1.6	2.9
Relative Dielectric Permittivity	9	10, 10, 13	6.5	3
Mobility of Electron (cm <sup>2</sup> /Vs)	20	20, 100, 35	2	10 <sup>-4</sup>
Mobility of Hole (cm <sup>2</sup> /Vs)	10	10, 25, 15	2	10 <sup>-4</sup>
Electron Affinity (eV)	4	4, 4, 4	3.9	2.2
Defect Density (cm <sup>-3</sup> )	10 <sup>15</sup>	10 <sup>15</sup> , 10 <sup>15</sup> , 10 <sup>16</sup>	2.5 × 10 <sup>15</sup>	10 <sup>15</sup>

**Table 2.** Device parameters set in the simulation.

Interface Defect Density [36,39,41]	
IL1 (ETL/Active Layer) Defect Density	2 × 10 <sup>9</sup> cm <sup>-2</sup>
IL2 (Active Layer/HTL) Defect Density	2 × 10 <sup>9</sup> cm <sup>-2</sup>
Back Metal Contact Properties [39–41]	
The electron work function of Au	−5.1 eV
Surface recombination velocity of the electron	10 <sup>5</sup> cm/s
Surface recombination velocity of hole	10 <sup>7</sup> cm/s
Front Metal Contact Properties [39–41]	
The electron work function of TCO	−4.4 eV
Surface recombination velocity electron	10 <sup>7</sup> cm/s
Surface recombination velocity of hole	10 <sup>5</sup> cm/s

Electron and hole pairs were generated when the photons were present on the perovskite material. The built-in electric field between the electrodes dissociates the electron-hole pair and transports it toward the respective electrodes. The current density–voltage (J–V) curves of the modelled structures are illustrated in Figure 11a–c. These make it clear that the change in the J<sub>sc</sub> and V<sub>oc</sub> values depends on the interaction between the perovskite material and the ETM. The CH<sub>3</sub>NH<sub>3</sub>PbI<sub>3</sub> and Cs<sub>2</sub>BiCuI<sub>6</sub> molecules display high PCE and J<sub>sc</sub> values in comparison to those of the other perovskite materials ((FA)<sub>2</sub>BiCuI<sub>6</sub> and (MA)<sub>2</sub>BiCuI<sub>6</sub>) as these molecules exhibit superior optical and transport properties, such as a high transport rate, a high absorption coefficient, and potentially dielectric properties. A detailed comparison of the performance parameters of different perovskite materials and the ETMS is listed in Table 3. Figure 12 shows a power conversion efficiency (PCE) comparison of all of the photo-harvesting and electron transport materials. Cs<sub>2</sub>BiCuI<sub>6</sub> with TiO<sub>2</sub>:CdS as an ETM outperforms all of the other double perovskite materials in terms of productivity.

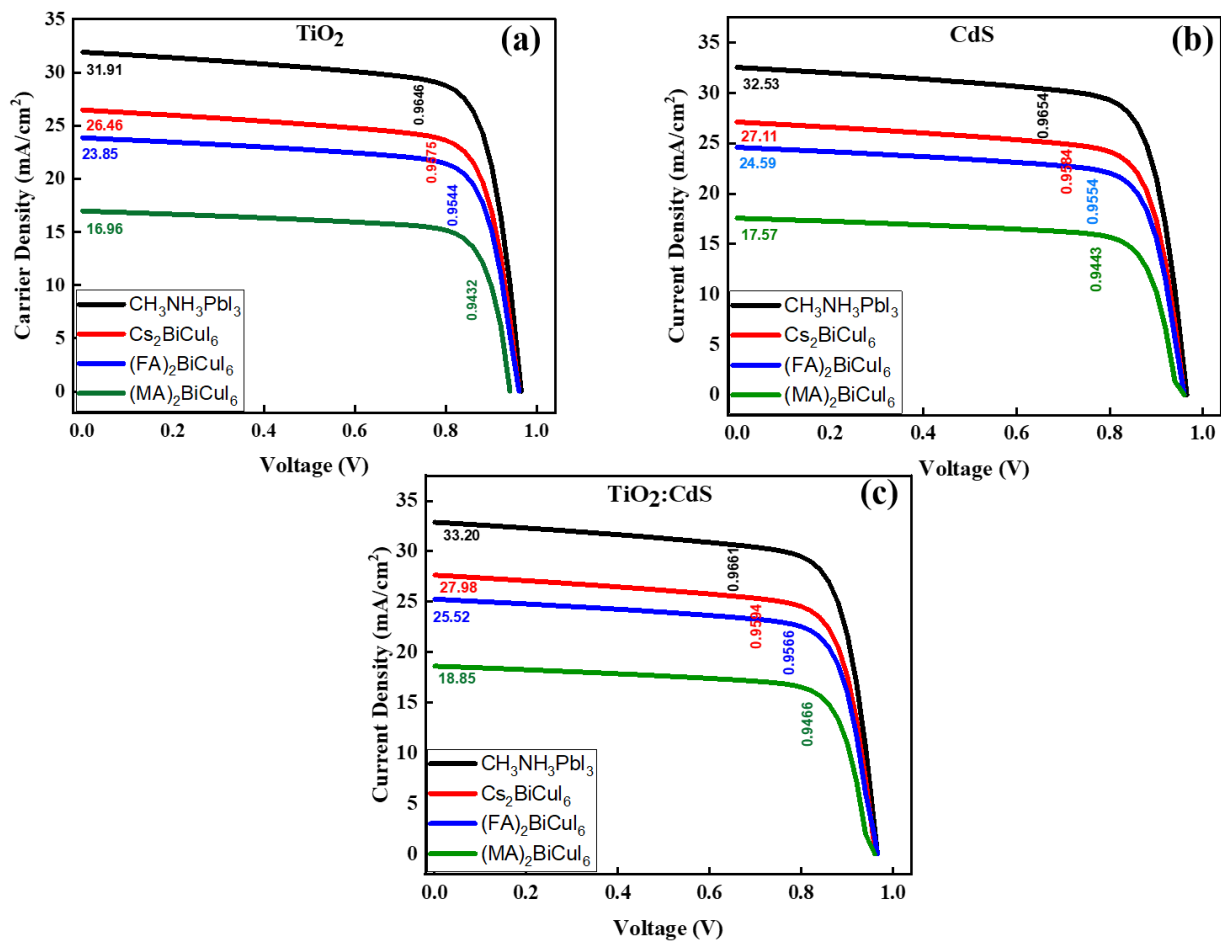
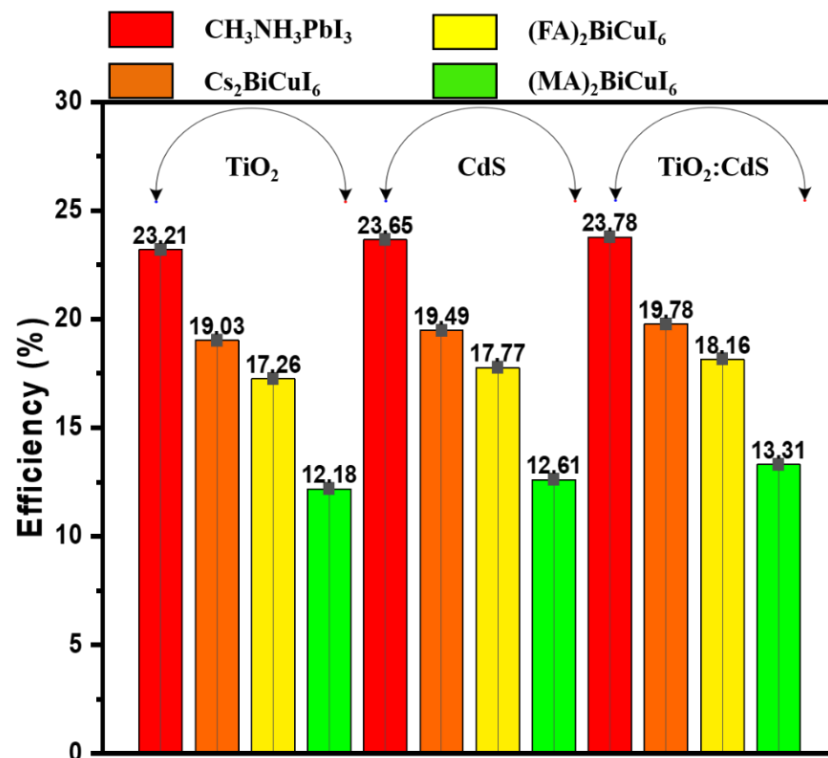


Figure 11. J–V Curve of different perovskite materials with ETM (a) TiO<sub>2</sub>, (b) CdS, and (c) TiO<sub>2</sub>:CdS.

Table 3. Performance comparison of different ETMs and perovskite material.

Active Materials	V <sub>oc</sub> (V)	J <sub>sc</sub> (mA/cm <sup>2</sup> )	FF (%)	PCE (%)
<b>TiO<sub>2</sub> as ETM</b>				
(MA) <sub>2</sub> BiCuI <sub>6</sub>	0.9432	16.96	76.14	12.18
(FA) <sub>2</sub> BiCuI <sub>6</sub>	0.9544	23.85	75.82	17.25
Cs <sub>2</sub> BiCuI <sub>6</sub>	0.9575	26.46	75.10	19.02
CH <sub>3</sub> NH <sub>3</sub> PbI <sub>3</sub>	0.9646	31.91	75.42	23.20
<b>CdS as ETM</b>				
(MA) <sub>2</sub> BiCuI <sub>6</sub>	0.9443	17.57	76.01	12.60
(FA) <sub>2</sub> BiCuI <sub>6</sub>	0.9554	24.59	75.65	17.76
Cs <sub>2</sub> BiCuI <sub>6</sub>	0.9584	27.11	75.03	19.48
CH <sub>3</sub> NH <sub>3</sub> PbI <sub>3</sub>	0.9654	32.53	75.32	23.64
<b>TiO<sub>2</sub>:CdS as ETM</b>				
(MA) <sub>2</sub> BiCuI <sub>6</sub>	0.9461	18.63	75.53	13.31
(FA) <sub>2</sub> BiCuI <sub>6</sub>	0.9561	25.25	75.25	18.16
Cs <sub>2</sub> BiCuI <sub>6</sub>	0.9589	27.65	74.62	19.77
CH <sub>3</sub> NH <sub>3</sub> PbI <sub>3</sub>	0.9656	32.88	74.93	23.78



**Figure 12.** Power conversion efficiency comparison of different ETMs and perovskite materials.

The interaction of double perovskite as a photoactive layer with TiO<sub>2</sub>:CdS is stronger than that of the other pairs, which results in the efficient extraction, transport, and collection of charge carriers towards the respective electrodes upon the application of light to the photoactive layer. Therefore, it yields better outcomes. The device output parameters such as the Voc, Jsc, FF, and PCE for CH<sub>3</sub>NH<sub>3</sub>PbI<sub>3</sub> and Cs<sub>2</sub>BiCuI<sub>6</sub>-based PSC are 0.9656 V and 0.9589 V, 32.88 mA/cm<sup>2</sup> and 27.65 mA/cm<sup>2</sup>, 74.93% and 74.62%, and 23.78% and 19.77%, respectively.

The quantum efficiency (QE) was measured as the ratio of the number of electrons created to the number of photons that were present on the photoactive layer. The QE curves for the different modelled structures are illustrated in Figure 13a–c. The QE graph is ideally a square wave, but it is sometimes reduced due to recombination, reflection losses, and other mechanisms such as surface passivation. It is also defined by the collection probability due to a single wavelength's generation profile. As a result, the QE is determined by the probability of the charge carriers being transported and extracted toward the respective electrodes. The variation in the QE curves of the different perovskite materials with different ETMs is due to the abovementioned losses. It was analyzed that the best QE value was obtained when TiO<sub>2</sub>:CdS was employed as ETM. This could be due to its preferable optoelectronic properties and superior interaction with the photo-harvesting material. It is also observed that the maximum values of the QE obtained for the different perovskite materials CH<sub>3</sub>NH<sub>3</sub>PbI<sub>3</sub>, Cs<sub>2</sub>BiCuI<sub>6</sub>, (FA)<sub>2</sub>BiCuI<sub>6</sub> and (MA)<sub>2</sub>BiCuI<sub>6</sub> with TiO<sub>2</sub>:CdS as an ETM are 77.23%, 76.57%, 75.71%, and 73.20%, respectively.

In addition, the numerical analysis of the designed perovskite solar cell (PSC) was also compared with the experimentally published data, which are shown in Table 4. It is analyzed that the results of the simulated device are close to the empirical findings reported in previously published research. Therefore, this work also provides theoretical insight for the future use of PSCs with increased productivity.

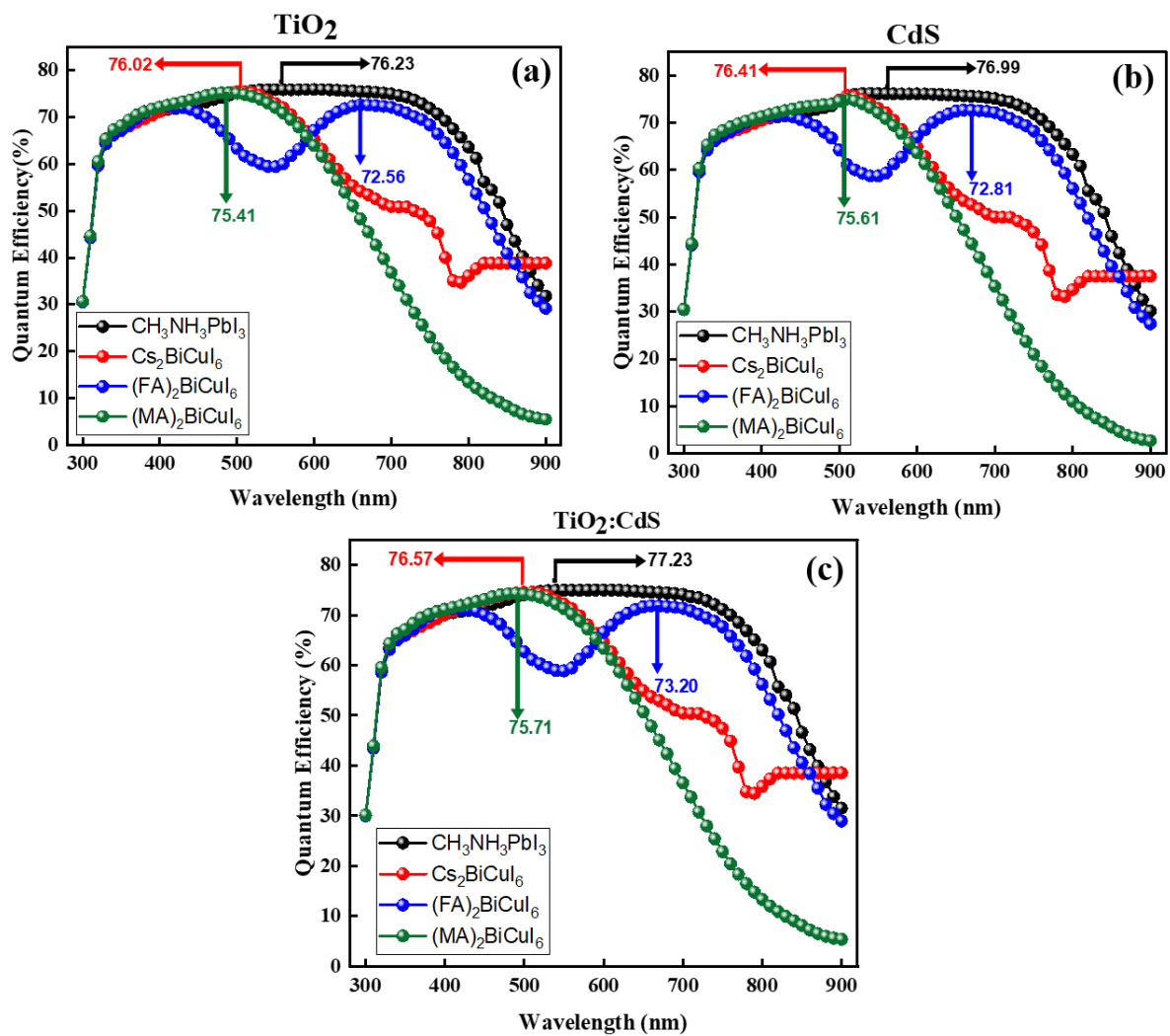


Figure 13. QE curve of different perovskite materials with ETM: (a)  $\text{TiO}_2$ , (b)  $\text{CdS}$ , and (c)  $\text{TiO}_2:\text{CdS}$ .

Table 4. Comparison of published work with simulated device designs.

Active Materials	$V_{oc}$ (V)	$J_{sc}$ ( $\text{mA}/\text{cm}^2$ )	FF (%)	PCE (%)	Ref.
<b>Experimental Results</b>					
SpiroMeOTAD/ $(\text{CH}_3\text{NH}_3\text{PbI}_3)/\text{TiO}_2:\text{Y}$	1.13	22.75	75.01	19.3	[90]
FAPbI <sub>3</sub>	1.06	24.4	77.5	20.1	[22]
Perovskite/ $\text{SnO}_2$	1.12	22.69	76.2	20.9	[91]
$\text{Cs}^+/\text{MA}^+/\text{FA}$ -mixing cations	1.16	24.0	75	21.1	[92]
LBSO/ $\text{CH}_3\text{NH}_3\text{PbI}_3$	1.07	23.4	78.6	21.2	[27]
Combined Silicon/Perovskite cells	1.08	16.5	74.1	23.0	[93]
<b>Simulation Results</b>					
$(\text{MA})_2\text{BiCuI}_6/\text{TiO}_2:\text{CdS}$	0.9461	18.63	75.53	13.31	This Study
$(\text{FA})_2\text{BiCuI}_6/\text{TiO}_2:\text{CdS}$	0.9561	25.25	75.25	18.16	This Study
$\text{Cs}_2\text{BiCuI}_6/\text{TiO}_2:\text{CdS}$	0.9589	27.65	74.62	19.77	This Study
$\text{CH}_3\text{NH}_3\text{PbI}_3/\text{TiO}_2:\text{CdS}$	0.9656	32.88	74.93	23.78	This Study

## 5. Conclusions

Herein, TiO<sub>2</sub>, CdS, and TiO<sub>2</sub>:CdS thin films were deposited onto a glass substrate by resistive heating thermal evaporation. Different spectroscopy and microscopy techniques were utilized for the thin film characterization. Material identification, photoluminescence studies, and optical characterizations were carried out using an FTIR, FS5 spectrofluorometer and UV-VIS spectroscopy, respectively. The FTIR results confirmed the formation of a TiO<sub>2</sub> bond with two sharper peaks at 670 cm<sup>-1</sup> and 522 cm<sup>-1</sup> and a CdS bond with a sharper peak at 748 cm<sup>-1</sup>. The highest transmittance value of 89% was observed in the visible region in the composite thin film. The optical band gap values for the deposited films (i.e., CdS, TiO<sub>2</sub>, TiO<sub>2</sub>:CdS) were 2.42 eV, 3.72 eV, and 3.6 eV, respectively. This variance may be attributed to the structural and morphological changes in the TiO<sub>2</sub> layer caused by the CdS content, as confirmed by XRD, optical, and SEM microscopy. The PL spectra showed several emission peaks at different wavelengths. Most of the peaks occurred in the visible region, which is primarily due to radiative, band-to-band recombination, and vacancy defects. The decrease in the material resistivity after the incorporation of CdS into TiO<sub>2</sub> was determined by the Van der Pauw method.

Additionally, the impact of the proposed ETMs on different perovskite materials was evaluated by numerical modelling. The simulation findings showed that TiO<sub>2</sub>:CdS has superior optoelectronic properties, resulting in a greater PCE than those of the other ETMs. The primary difficulty in obtaining PSC technology is developing improved absorber materials with high efficiency, high stability, and low-cost manufacturing properties. This paper also presents a framework for efficiently utilizing different absorbers, notably Cs<sub>2</sub>BiCuI<sub>6</sub>, in PSC device designs.

**Author Contributions:** Conceptualization, G.A.N.; Resources, S.S.H. and G.A.N.; methodology, A.Z., G.A.N. and A.S.; software, A.Z., G.A.N. and M.R.; formal analysis, M.K., G.A.N., A.Z. and A.A.S.; writing—original draft preparation, A.Z., G.A.N. and A.A.S.; writing—review and editing, G.A.N., M.R., S.N.S.B. and S.S.H.; project administration, S.S.H., M.A.S. and A.A.; funding acquisition, M.A.S. and A.A. All authors have read and agreed to the published version of the manuscript.

**Funding:** This research was funded by the Researchers Supporting Project (RSP-2023R269) at King Saud University, Riyadh, Saudi Arabia.

**Data Availability Statement:** The data presented in this study are available from the corresponding author upon request.

**Acknowledgments:** The authors would like to acknowledge the Researcher's Supporting Project Number (RSP2023R269), King Saud University, Riyadh, Saudi Arabia, for their support in this work.

**Conflicts of Interest:** The authors declare no conflict of interest.

## Abbreviations

TiO<sub>2</sub>: Titanium dioxide; CdS: Cadmium Sulfide; LEDs: Light Emitting Diodes; CVD: Chemical Vapor Deposition; PVD: Physical Vapor Deposition; ETM: Electron Transport Material; TCO: Transparent Conducting Oxide Film; PV: Photovoltaic; PSCs: Perovskite Solar Cells; PCE: Power Conversion Efficiency; 1D: One dimensional; ZnO: Zinc Oxide; SnO<sub>2</sub>: Tin Dioxide; ETMs: Electron Transport Materials; PSC: Perovskite Solar Cell; Zn<sub>2</sub>SnO<sub>4</sub>: Zinc Stannate; BaSnO<sub>3</sub>: Barium Tin Trioxide; CIGS: Copper indium gallium (di)selenide; CdTe: Cadmium Telluride; CuI: Copper Iodide; IPA: Isopropyl Alcohol; g: gram; A: Ampere; UV-Vis: Ultraviolet-Visible; nm: Nanometer; FTIR: Fourier Transform Infrared Spectroscopy; cm<sup>-1</sup>: per centimeter; CCD: Charge-Coupled Device; VDP: Van der Pauw; HTL: Hole Transport Layer; ETL: Electron Transport Layer; FTO: Au: Gold; %: Percentage; α: Absorption coefficient; h: Planck's constant; ν: frequency; Eg: Energy gap; eV: Electron Volt; Cd: Cadmium; S: Sulphur; Ti: Titanium; O: Oxygen; PL: Photoluminescence; cm: Centimeter; CH<sub>3</sub>NH<sub>3</sub>PbI<sub>3</sub>: Methyl ammonium lead iodide; Cs<sub>2</sub>BiCuI<sub>6</sub>: Cesium bismuth copper iodide; (FA)<sub>2</sub>BiCuI<sub>6</sub>: Formamidinium bismuth copper iodide; (MA)<sub>2</sub>BiCuI<sub>6</sub>: Methyl ammonium bismuth copper iodide; HTM: Hole Transport Material; J: Current Density; V: voltage; J<sub>sc</sub>: Short Circuit Density; V<sub>oc</sub>: Open Circuit Voltage; FF: Fill Factor; N<sub>2</sub>: Nitrogen gas; cm<sup>-3</sup>: Per Cubic Centimeter.

## References

1. Bhatti, M.A.; Shah, A.A.; Almaani, K.F.; Tahira, A.; Chandio, A.D.; Willander, M.; Nur, O.; Mugheri, A.Q.; Bhatti, A.L.; Waryani, B.; et al. TiO<sub>2</sub>/ZnO Nanocomposite Material for Efficient Degradation of Methylene Blue. *J. Nanosci. Nanotechnol.* **2021**, *21*, 2511–2519. [[CrossRef](#)]
2. Bhatti, M.A.; Gilani, S.J.; Shah, A.A.; Channa, I.A.; Almani, K.F.; Chandio, A.D.; Halepoto, I.A.; Tahira, A.; Bin Jumah, M.N.; Ibupoto, Z.H. Effective Removal of Methylene Blue by Surface Alteration of TiO<sub>2</sub> with Ficus Carica Leaf Extract under Visible Light. *Nanomaterials* **2022**, *12*, 2766. [[CrossRef](#)]
3. Hoffmann, M.R.; Martin, S.T.; Choi, W.; Bahnemann, D.W. Environmental applications of semiconductor photocatalysis. *Chem. Rev.* **1995**, *95*, 69–96. [[CrossRef](#)]
4. Thompson, T.L.; Yates, J.T. Surface science studies of the photoactivation of TiO<sub>2</sub> new photochemical processes. *Chem. Rev.* **2006**, *106*, 4428–4453. [[CrossRef](#)]
5. Tan, J.; Liu, L.; Li, F.; Chen, Z.; Chen, G.Y.; Fang, F.; Jinsong, G.; Miao, H.; Xiaohong, Z. Screening of Endocrine Disrupting Potential of Surface Waters via an Affinity-Based Biosensor in a Rural Community in the Yellow River Basin, China. *Environ. Sci. Technol.* **2022**, *56*, 14350–14360.
6. Baron Jaimes, A.; Jaramillo-Quintero, O.A.; Miranda Gamboa, R.A.; Medina-Flores, A.; Rincon, M.E. Functional ZnO/TiO<sub>2</sub> Bilayer as Electron Transport Material for Solution-Processed Sb<sub>2</sub>S<sub>3</sub> Solar Cells. *Sol. RRL* **2021**, *5*, 2000764. [[CrossRef](#)]
7. Li, H.; Wang, X.; Xu, J.; Zhang, Q.; Bando, Y.; Golberg, D.; Ma, Y.; Zhai, T. One-dimensional CdS nanostructures: A promising candidate for optoelectronics. *Adv. Mater.* **2013**, *25*, 3017–3037. [[CrossRef](#)]
8. Hullavarad, N.; Karulkar, P. Cadmium sulphide (CdS) nanotechnology: Synthesis and applications. *J. Nanosci. Nanotechnol.* **2008**, *8*, 3272–3299. [[CrossRef](#)]
9. Müller, J.; Kluth, O.; Wieder, S.; Siekmann, H.; Schöpe, G.; Reetz, W.; Vetterl, O.; Lundszen, D.; Lambert, A.; Finger, F.; et al. Development of highly efficient thin film silicon solar cells on texture-etched zinc oxide-coated glass substrates. *Sol. Energy Mater. Sol. Cells* **2001**, *66*, 275–281. [[CrossRef](#)]
10. Yu, F. *Internal Polarization Effect in Perovskite Solar Cells*; University of Pittsburgh: Pittsburgh, PA, USA, 2016.
11. Conings, B.; Baeten, L.; Jacobs, T.; Dera, R.; D’Haen, J.; Manca, J.; Boyen, H.G. An easy-to-fabricate low-temperature TiO<sub>2</sub> electron collection layer for high efficiency planar heterojunction perovskite solar cells. *APL Mater.* **2014**, *2*, 081505. [[CrossRef](#)]
12. Liu, D.; Kelly, T.L. Perovskite solar cells with a planar heterojunction structure prepared using room-temperature solution processing techniques. *Nat. Photonics* **2014**, *8*, 133–138. [[CrossRef](#)]
13. Kojima, A.; Teshima, K.; Miyasaka, T.; Shirai, Y. Novel photoelectrochemical cell with mesoscopic electrodes sensitized by lead-halide compounds (2). In *ECS Meeting Abstracts*; IOP Publishing: Bristol, UK, 2006.
14. Kojima, A.; Teshima, K.; Shirai, Y.; Miyasaka, T. Organometal halide perovskites as visible-light sensitizers for photovoltaic cells. *J. Am. Chem. Soc.* **2009**, *131*, 6050–6051. [[CrossRef](#)] [[PubMed](#)]
15. Im, J.H.; Lee, C.R.; Lee, J.W.; Park, S.W.; Park, N.G. 6.5% efficient perovskite quantum-dot-sensitized solar cell. *Nanoscale* **2011**, *3*, 4088–4093. [[CrossRef](#)]
16. Anttu, N. Shockley–Queisser detailed balance efficiency limit for nanowire solar cells. *ACS Photonics* **2015**, *2*, 446–453. [[CrossRef](#)]
17. Sha, W.E.; Ren, X.; Chen, L.; Choy, W.C. The efficiency limit of CH<sub>3</sub>NH<sub>3</sub>PbI<sub>3</sub> perovskite solar cells. *Appl. Phys. Lett.* **2015**, *106*, 221104. [[CrossRef](#)]
18. Law, M.; Greene, L.E.; Johnson, J.C.; Saykally, R.; Yang, P. Nanowire dye-sensitized solar cells. *Nat. Mater.* **2005**, *4*, 455–459. [[CrossRef](#)]
19. Lv, Y.; Cai, B.; Wu, Y.; Wang, S.; Jiang, Q.; Ma, Q.; Liu, J.J.; Zhang, W.H. High performance perovskite solar cells using TiO<sub>2</sub> nanospindles as ultrathin mesoporous layer. *J. Energy Chem.* **2018**, *27*, 951–956. [[CrossRef](#)]
20. Yang, G.; Tao, H.; Qin, P.; Ke, W.; Fang, G. Recent progress in electron transport layers for efficient perovskite solar cells. *J. Mater. Chem. A* **2016**, *4*, 3970–3990. [[CrossRef](#)]
21. Jeon, N.J.; Noh, J.H.; Kim, Y.C.; Yang, W.S.; Ryu, S.; Seok, S.I. Solvent engineering for high-performance inorganic–organic hybrid perovskite solar cells. *Nat. Mater.* **2014**, *13*, 897–903. [[CrossRef](#)]
22. Yang, W.S.; Noh, J.H.; Jeon, N.J.; Kim, Y.C.; Ryu, S.; Seo, J.; Seok, S.I. High-performance photovoltaic perovskite layers fabricated through intramolecular exchange. *Science* **2015**, *348*, 1234–1237. [[CrossRef](#)]
23. Song, J.; Zheng, E.; Bian, J.; Wang, X.F.; Tian, W.; Sanehira, Y.; Miyasaka, T. Low-temperature SnO<sub>2</sub>-based electron selective contact for efficient and stable perovskite solar cells. *J. Mater. Chem. A* **2015**, *3*, 10837–10844. [[CrossRef](#)]
24. Kumar, M.H.; Yantara, N.; Dharani, S.; Graetzel, M.; Mhaisalkar, S.; Boix, P.P.; Mathews, N. Flexible, low-temperature, solution processed ZnO-based perovskite solid state solar cells. *Chem. Commun.* **2013**, *49*, 11089–11091. [[CrossRef](#)]
25. Son, D.Y.; Im, J.H.; Kim, H.S.; Park, N.G. 11% efficient perovskite solar cell based on ZnO nanorods: An effective charge collection system. *J. Phys. Chem. C* **2014**, *118*, 16567–16573. [[CrossRef](#)]
26. Mali, S.S.; Shim, C.S.; Kim, H.; Patil, P.S.; Hong, C.K. In situ processed gold nanoparticle-embedded TiO<sub>2</sub> nanofibers enabling plasmonic perovskite solar cells to exceed 14% conversion efficiency. *Nanoscale* **2016**, *8*, 2664–2677. [[CrossRef](#)]
27. Shin, S.S.; Yeom, E.J.; Yang, W.S.; Hur, S.; Kim, M.G.; Im, J.; Seo, J.; Noh, J.H.; Seok, S.I. Colloidally prepared La-doped BaSnO<sub>3</sub> electrodes for efficient, photostable perovskite solar cells. *Science* **2017**, *356*, 167–171. [[CrossRef](#)]
28. Zhu, J.; Liu, X.; Geier, M.L.; McMorro, J.J.; Jariwala, D.; Beck, M.E.; Huang, W.; Marks, T.J.; Hersam, M.C. Layer-by-layer assembled 2D montmorillonite dielectrics for solution-processed electronics. *Adv. Mater.* **2016**, *28*, 63–68. [[CrossRef](#)]

29. Xie, H.; Yin, X.; Liu, J.; Guo, Y.; Chen, P.; Que, W.; Wang, G.; Gao, B. Low temperature solution-derived TiO<sub>2</sub>-SnO<sub>2</sub> bilayered electron transport layer for high performance perovskite solar cells. *Appl. Surf. Sci.* **2019**, *464*, 700–707. [\[CrossRef\]](#)
30. Xu, X.; Zhang, H.; Shi, J.; Dong, J.; Luo, Y.; Li, D.; Meng, Q. Highly efficient planar perovskite solar cells with a TiO<sub>2</sub>/ZnO electron transport bilayer. *J. Mater. Chem. A* **2015**, *3*, 19288–19293. [\[CrossRef\]](#)
31. Chai, W.; Zhu, W.; Chen, D.; Chen, D.; Xi, H.; Chang, J.; Zhang, J.; Zhang, C.; Hao, Y. Combustion-processed NiO/ALD TiO<sub>2</sub> bilayer as a novel low-temperature electron transporting material for efficient all-inorganic CsPbI<sub>3</sub> solar cell. *Sol. Energy* **2020**, *203*, 10–18. [\[CrossRef\]](#)
32. Dunlap-Shohl, W.A.; Younts, R.; Gautam, B.; Gundogdu, K.; Mitzi, D.B. Effects of Cd diffusion and doping in high-performance perovskite solar cells using CdS as electron transport layer. *J. Phys. Chem. C* **2016**, *120*, 16437–16445. [\[CrossRef\]](#)
33. Wessendorf, C.D.; Hanisch, J.; Müller, D.; Ahlswede, E. CdS as Electron Transport Layer for Low-Hysteresis Perovskite Solar Cells. *Sol. RRL* **2018**, *2*, 1800056. [\[CrossRef\]](#)
34. Luo, C.; Jiang, P.; Hu, L.; Bian, M.; Wan, L.; Niu, H.; Mao, X.; Zhou, R.; Xu, J. Constructing CdS-Based Electron Transporting Layers With Efficient Electron Extraction for Perovskite Solar Cells. *IEEE J. Photovolt.* **2021**, *11*, 1014–1021. [\[CrossRef\]](#)
35. Gu, Z.; Chen, F.; Zhang, X.; Liu, Y.; Fan, C.; Wu, G.; Li, H.; Chen, H. Novel planar heterostructure perovskite solar cells with CdS nanorods array as electron transport layer. *Sol. Energy Mater. Sol. Cells* **2015**, *140*, 396–404. [\[CrossRef\]](#)
36. Lin, L.; Jiang, L.; Qiu, Y.; Yu, Y. Modeling and analysis of HTM-free perovskite solar cells based on ZnO electron transport layer. *Superlattices Microstruct.* **2017**, *104*, 167–177. [\[CrossRef\]](#)
37. Chakraborty, K.; Choudhury, M.G.; Paul, S. Numerical study of Cs<sub>2</sub>TiX<sub>6</sub> (X = Br<sup>-</sup>, I<sup>-</sup>, F<sup>-</sup> and Cl<sup>-</sup>) based perovskite solar cell using SCAPS-1D device simulation. *Sol. Energy* **2019**, *194*, 886–892. [\[CrossRef\]](#)
38. Karthick, S.; Velumani, S.; Bouclé, J. Experimental and SCAPS simulated formamidinium perovskite solar cells: A comparison of device performance. *Sol. Energy* **2020**, *205*, 349–357. [\[CrossRef\]](#)
39. Nowsherwan, G.A.; Hussain, S.S.; Khan, M.; Haider, S.; Akbar, I.; Nowsherwan, N.; Ikram, S.; Ishtiaq, S.; Riaz, S.; Naseem, S. Role of graphene-oxide and reduced-graphene-oxide on the performance of lead-free double perovskite solar cell. *Zeitschrift für Naturforschung A* **2022**, *77*, 1083–1098. [\[CrossRef\]](#)
40. Abdelaziz, S.; Zekry, A.; Shaker, A.; Abouelatta, M. Investigating the performance of formamidinium tin-based perovskite solar cell by SCAPS device simulation. *Opt. Mater.* **2020**, *101*, 109738. [\[CrossRef\]](#)
41. Hussain, S.S.; Riaz, S.; Nowsherwan, G.A.; Jahangir, K.; Raza, A.; Iqbal, M.J.; Sadiq, I.; Hussain, S.M.; Naseem, S. Numerical modeling and optimization of lead-free hybrid double perovskite solar cell by using SCAPS-1D. *J. Renew. Energy* **2021**, *2021*, 6668687. [\[CrossRef\]](#)
42. Kumar, M.; Raj, A.; Kumar, A.; Anshul, A. An optimized lead-free formamidinium Sn-based perovskite solar cell design for high power conversion efficiency by SCAPS simulation. *Opt. Mater.* **2020**, *108*, 110213. [\[CrossRef\]](#)
43. Samiul Islam, M.; Sobayel, K.; Al-Kahtani, A.; Islam, M.A.; Muhammad, G.; Amin, N.; Shahiduzzaman, M.; Akhtaruzzaman, M. Defect study and modelling of SnX<sub>3</sub>-based perovskite solar cells with SCAPS-1D. *Nanomaterials* **2021**, *11*, 1218. [\[CrossRef\]](#)
44. Haider, S.Z.; Anwar, H.; Wang, M. A comprehensive device modelling of perovskite solar cell with inorganic copper iodide as hole transport material. *Semicond. Sci. Technol.* **2018**, *33*, 035001. [\[CrossRef\]](#)
45. Chen, W.-K. *Fundamentals of Circuits and Filters*; CRC Press: Boca Raton, FL, USA, 2018.
46. Lisičar Vukušić, J. *Multidisciplinary Approach in Industrial Baker's Yeast Production: From Manufacture to Integrated Sustainability*; Institutionelles Repositorium der Leibniz Universität Hannover: Hannover, Germany, 2019.
47. Förster, H. *UV/vis spectroscopy. Molecular Sieves—Science and Technology*; Characterization I; Springer: Berlin/Heidelberg, Germany, 2004; pp. 337–426.
48. Picollo, M.; Aceto, M.; Vitorino, T. UV-Vis spectroscopy. *Phys. Sci. Rev.* **2019**, *4*. [\[CrossRef\]](#)
49. Ennaoui, A.; Sankapal, B.R.; Skryshevsky, V.; Lux-Steiner, M.C. TiO<sub>2</sub> and TiO<sub>2</sub>-SiO<sub>2</sub> thin films and powders by one-step soft-solution method: Synthesis and characterizations. *Sol. Energy Mater. Sol. Cells* **2006**, *90*, 1533–1541. [\[CrossRef\]](#)
50. Purkayastha, D.D.; Krishna, M.G. Dopant controlled photoinduced hydrophilicity and photocatalytic activity of SnO<sub>2</sub> thin films. *Appl. Surf. Sci.* **2018**, *447*, 724–731.
51. Noh, Y.W.; Jin, I.S.; Kim, K.S.; Park, S.H.; Jung, J.W. Reduced energy loss in SnO<sub>2</sub>/ZnO bilayer electron transport layer-based perovskite solar cells for achieving high efficiencies in outdoor/indoor environments. *J. Mater. Chem. A* **2020**, *8*, 17163–17173. [\[CrossRef\]](#)
52. De Sá, R.G.; Arantes, T.M.; de Macedo, E.F.; Dona, L.M.; Pereira, J.C.; Hurtado, C.R.; Varghese, R.J. Photoprotective activity of zirconia nanoparticles. *Colloids Surf. B: Biointerfaces* **2021**, *202*, 111636. [\[CrossRef\]](#)
53. Hassan, Q.M.; Manshad, R. Surface morphology and optical limiting properties of azure B doped PMMA film. *Opt. Mater.* **2019**, *92*, 22–29. [\[CrossRef\]](#)
54. Bota, V.B.; Turcus, V.; Mihali, C.V.; Arsene, G.G.; Ivănescu, L.C.; Zamfirache, M.M. Anatomical investigations on *Oenothera biennis* L. using optical microscopy and scanning electron microscopy (SEM). *Res. J. Agric. Sci.* **2020**, *52*, 11.
55. Ramadan, A.; Gould, R.; Ashour, A. On the Van der Pauw method of resistivity measurements. *Thin Solid Film.* **1994**, *239*, 272–275. [\[CrossRef\]](#)
56. L Liu, F.; Zhu, J.; Wei, J.; Li, Y.; Lv, M.; Yang, S.; Zhang, B.; Yao, J.; Dai, S. Numerical simulation: Toward the design of high-efficiency planar perovskite solar cells. *Appl. Phys. Lett.* **2014**, *104*, 253508. [\[CrossRef\]](#)

57. Burgelman, M.; Nollet, P.; Degraeve, S. Modelling polycrystalline semiconductor solar cells. *Thin Solid Film.* **2000**, *361*, 527–532. [[CrossRef](#)]
58. Mohsin, A.K.; Bidin, N. Effect of CdS thickness on the optical and structural properties of TiO<sub>2</sub>/CdS nanocomposite film. In *Advanced Materials Research*; Trans Tech Publications Ltd.: Zurich, Switzerland, 2015.
59. Shi, J.W.; Yan, X.; Cui, H.J.; Zong, X.; Fu, M.L.; Chen, S.; Wang, L. Low-temperature synthesis of CdS/TiO<sub>2</sub> composite photocatalysts: Influence of synthetic procedure on photocatalytic activity under visible light. *J. Mol. Catal. A Chem.* **2012**, *356*, 53–60. [[CrossRef](#)]
60. Ripathi, A.K.; Singh, M.K.; Mathpal, M.C.; Mishra, S.K.; Agarwal, A. Study of structural transformation in TiO<sub>2</sub> nanoparticles and its optical properties. *J. Alloys Compd.* **2013**, *549*, 114–120. [[CrossRef](#)]
61. Ramadan, R.; Manso-Silvan, M.; Martın-Palma, R.J. Hybrid porous silicon/silver nanostructures for the development of enhanced photovoltaic devices. *J. Mater. Sci.* **2020**, *55*, 5458–5470. [[CrossRef](#)]
62. Chrysicopoulou, P.; Davazoglou, D.; Trapalis, C.; Kordas, G. Optical properties of very thin (<100 nm) sol–gel TiO<sub>2</sub> films. *Thin Solid Film.* **1998**, *323*, 188–193.
63. Sahay, P.P.; Nath, R.K.; Tewari, S. Optical properties of thermally evaporated CdS thin films. *Cryst. Res. Technol. J. Exp. Ind. Crystallogr.* **2007**, *42*, 275–280. [[CrossRef](#)]
64. Thamaphat, K.; Limsuwan, P.; Ngotawornchai, B. Phase characterization of TiO<sub>2</sub> powder by XRD and TEM. *Agric. Nat. Resour.* **2008**, *42*, 357–361.
65. Vishwas, M.; Shamala, K.S.; Gandla, S.B. Comparison of optical properties of CdS thin films synthesized by spray pyrolysis and thermal evaporation method. *J. Opt.* **2022**, *51*, 736–740. [[CrossRef](#)]
66. Kumar, S.; Sharma, J.K. Stable phase CdS nanoparticles for optoelectronics: A study on surface morphology, structural and optical characterization. *Mater. Sci. Pol.* **2016**, *34*, 368–373. [[CrossRef](#)]
67. Esakkiraj, E.; Kadhar, S.S.A.; Henry, J.; Mohanraj, K.; Kannan, S.; Barathan, S.; Sivakumar, G. Optostructural and vibrational characteristics of Cu:CdS nanoparticles by precipitation method. *Optik* **2013**, *124*, 5229–5231. [[CrossRef](#)]
68. Slam, M.A.; Haque, F.; Rahman, K.S.; Dhar, N.; Hossain, M.S.; Sulaiman, Y.; Amin, N. Effect of oxidation on structural, optical and electrical properties of CdS thin films grown by sputtering. *Optik* **2015**, *126*, 3177–3180.
69. Nam, S.-H.; Cho, S.-J.; Boo, J.-H. Growth behavior of titanium dioxide thin films at different precursor temperatures. *Nanoscale Res. Lett.* **2012**, *7*, 89. [[CrossRef](#)] [[PubMed](#)]
70. Haider, A.J.; Thamir, A.D.; Najim, A.A.; Ali, G.A. Improving efficiency of TiO<sub>2</sub>: Ag/Si solar cell prepared by pulsed laser deposition. *Plasmonics* **2017**, *12*, 105–115. [[CrossRef](#)]
71. Abdullah, S.A.; Sahdan, M.Z.; Nafarizal, N.; Saim, H.; Bakri, A.S.; Rohaida, C.C.; Adriyanto, F.; Sari, Y. Photoluminescence study of trap-state defect on TiO<sub>2</sub> thin films at different substrate temperature via RF magnetron sputtering. *J. Phys. Conf. Ser.* **2018**, *995*, 012067. [[CrossRef](#)]
72. Ohta, S.; Sekiya, T.; Kurita, S. Pressure dependence of optical properties of anatase TiO<sub>2</sub> single crystal. *Phys. Status Solidi B* **2001**, *223*, 265–269. [[CrossRef](#)]
73. Abazović, N.D.; Čomor, M.I.; Dramićanin, M.D.; Jovanović, D.J.; Ahrenkiel, S.P.; Nedeljković, J.M. Photoluminescence of anatase and rutile TiO<sub>2</sub> particles. *J. Phys. Chem. B* **2006**, *110*, 25366–25370. [[CrossRef](#)]
74. Daude, N.; Gout, C.; Jouanin, C. Electronic band structure of titanium dioxide. *Phys. Rev. B* **1977**, *15*, 3229. [[CrossRef](#)]
75. Pham, H.H.; Wang, L.-W. Oxygen vacancy and hole conduction in amorphous TiO<sub>2</sub>. *Phys. Chem. Chem. Phys.* **2015**, *17*, 541–550. [[CrossRef](#)]
76. Rajabi, M.; Shogh, S. Defect study of TiO<sub>2</sub> nanorods grown by a hydrothermal method through photoluminescence spectroscopy. *J. Lumin.* **2015**, *157*, 235–242. [[CrossRef](#)]
77. Rahman, M.M.; Krishna, K.M.; Soga, T.; Jimbo, T.; Umeno, M. Optical properties and X-ray photoelectron spectroscopic study of pure and Pb-doped TiO<sub>2</sub> thin films. *J. Phys. Chem. Solids* **1999**, *60*, 201–210. [[CrossRef](#)]
78. Tang, H.; Prasad, K.; Sanjines, R.; Schmid, P.E.; Levy, F. Electrical and optical properties of TiO<sub>2</sub> anatase thin films. *J. Appl. Phys.* **1994**, *75*, 2042–2047. [[CrossRef](#)]
79. Chandekar, K.V.; Shkir, M.; Alshahrani, T.; Khan, A.; AlFaify, S. An in-depth investigation of physical properties of Nd doped CdS thin films for optoelectronic applications. *Chin. J. Phys.* **2020**, *67*, 681–694. [[CrossRef](#)]
80. Islam, M.A.; Misran, H.; Akhtaruzzaman, M.; Amin, N. Influence of oxygen on structural and optoelectronic properties of CdS thin film deposited by magnetron sputtering technique. *Chin. J. Phys.* **2020**, *67*, 170–179. [[CrossRef](#)]
81. Kim, D.; Park, Y.; Kim, M.; Choi, Y.; Park, Y.S.; Lee, J. Optical and structural properties of sputtered CdS films for thin film solar cell applications. *Mater. Res. Bull.* **2015**, *69*, 78–83. [[CrossRef](#)]
82. Tan, K.; Lin, P.; Wang, G.; Liu, Y.; Xu, Z.; Lin, Y. Controllable design of solid-state perovskite solar cells by SCAPS device simulation. *Solid-State Electron.* **2016**, *126*, 75–80. [[CrossRef](#)]
83. Moreh, A.U.; Momoh, M.; Hamza, B.; Abdullahi, S.; Yahya, H.N.; Namadi, S.; Umar, S. Influence of Substrate Temperature on Electrical Resistivity and Surface Morphology of CuAlS<sub>2</sub> Thin Films Prepared by Vacuum Thermal Evaporation Method. *UDUS Open Educ. Resour.* **2014**, *3*, 45–147.
84. Pham, H.Q.; Holmes, R.J.; Aydil, E.S.; Gagliardi, L. Lead-free double perovskites Cs<sub>2</sub>InCuCl<sub>6</sub> and (CH<sub>3</sub>NH<sub>3</sub>)<sub>2</sub>InCuCl<sub>6</sub>: Electronic, optical, and electrical properties. *Nanoscale* **2019**, *11*, 11173–11182. [[CrossRef](#)]

85. Seck, S.M.; Ndiaye, E.N.; Fall, M.; Charvet, S. Study of Efficiencies CdTe/CdS Photovoltaic Solar Cell According to Electrical Properties by Scaps Simulation. *Nat. Resour.* **2020**, *11*, 147–155. [[CrossRef](#)]
86. Ball, J.M.; Stranks, S.D.; Hörantner, M.T.; Hüttner, S.; Zhang, W.; Crossland, E.J.; Ramirez, I.; Riede, M.; Johnston, M.B.; Friend, R.H.; et al. Optical properties and limiting photocurrent of thin-film perovskite solar cells. *Energy Environ. Sci.* **2015**, *8*, 602–609. [[CrossRef](#)]
87. Roknuzzaman, M.; Zhang, C.; Ostrikov, K.K.; Du, A.; Wang, H.; Wang, L.; Tesfamichael, T. Electronic and optical properties of lead-free hybrid double perovskites for photovoltaic and optoelectronic applications. *Sci. Rep.* **2019**, *9*, 718. [[CrossRef](#)] [[PubMed](#)]
88. Banyamin, Z.Y.; Kelly, P.J.; West, G.; Boardman, J. Electrical and optical properties of fluorine doped tin oxide thin films prepared by magnetron sputtering. *Coatings* **2014**, *4*, 732–746. [[CrossRef](#)]
89. Filipič, M.; Löper, P.; Niesen, B.; De Wolf, S.; Krč, J.; Ballif, C.; Topič, M. CH<sub>3</sub>NH<sub>3</sub>PbI<sub>3</sub> perovskite/silicon tandem solar cells: Characterization based optical simulations. *Opt. Express* **2015**, *23*, A263–A278. [[CrossRef](#)] [[PubMed](#)]
90. Zhou, H.; Chen, Q.; Li, G.; Luo, S.; Song, T.B.; Duan, H.S.; Hong, Z.; You, J.; Liu, Y.; Yang, Y. Interface engineering of highly efficient perovskite solar cells. *Science* **2014**, *345*, 542–546. [[CrossRef](#)] [[PubMed](#)]
91. Saliba, M.; Matsui, T.; Seo, J.Y.; Domanski, K.; Correa-Baena, J.P.; Nazeeruddin, M.K.; Zakeeruddin, S.; Tress, W.; Abate, A.; Hagfeldt, A.; et al. Cesium-containing triple cation perovskite solar cells: Improved stability, reproducibility and high efficiency. *Energy Environ. Sci.* **2016**, *9*, 1989–1997. [[CrossRef](#)]
92. Taherianfard, H.; Kim, G.; Byranvand, M.; Choi, K.; Kang, G.; Choi, H.; Tajabadi, F.; Taghavinia, N.; Park, T. Effective Management of Nucleation and Crystallization Processes in Perovskite Formation via Facile Control of Antisolvent Temperature. *ACS Appl. Energy Mater.* **2020**, *3*, 1506–1514. [[CrossRef](#)]
93. Chen, B.; Bai, Y.; Yu, Z.; Li, T.; Zheng, X.; Dong, Q.; Shen, L.; Boccard, M.; Gruverman, A.; Holman, Z.; et al. Efficient semitransparent perovskite solar cells for 23.0%-efficiency perovskite/silicon four-terminal tandem cells. *Adv. Energy Mater.* **2016**, *6*, 1601128. [[CrossRef](#)]

**Disclaimer/Publisher's Note:** The statements, opinions and data contained in all publications are solely those of the individual author(s) and contributor(s) and not of MDPI and/or the editor(s). MDPI and/or the editor(s) disclaim responsibility for any injury to people or property resulting from any ideas, methods, instructions or products referred to in the content.